J. Fluid Mech. (2022), *vol*. 951, A47, doi:10.1017/jfm.2022.905

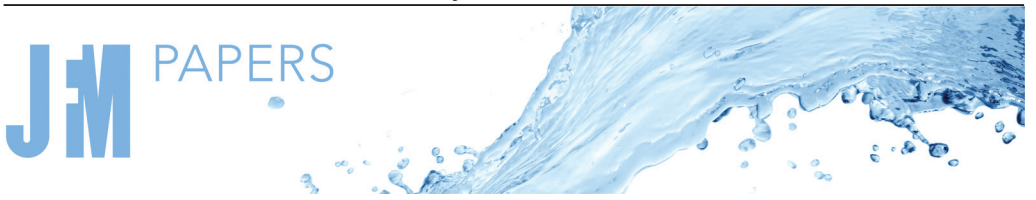

Evolution of two counter-rotating vortices in a stratified turbulent environment

Yuanwei Bin[1,2,†], Xiang I.A. Yang[1], Yantao Yang[2,3], Rui Ni[4] and Yipeng Shi[2]

[1]Mechanical Engineering, Pennsylvania State University, Pennsylvania 16802, USA

[2]State Key Laboratory for Turbulence and Complex Systems and Department of Mechanics and Engineering Science, College of Engineering, Peking University, Beijing 100871, PR China

[3]Joint Laboratory of Marine Hydrodynamics and Ocean Engineering, Pilot National Laboratory for Marine Science and Technology (Qingdao), Shandong 266299, PR China

[4]Mechanical Engineering, Johns Hopkins University, Maryland 21218, USA

(Received 26 May 2022; revised 14 September 2022; accepted 20 October 2022)

We conduct direct numerical simulations and study the evolution of a pair of counter-rotating vortices in a stratified and turbulent environment beyond the first vortex linking (which is due to the Crow instability). The initial position of the two vortices is perpendicular to the direction of thermal stratification. We vary the Froude number, the background turbulence intensity and the Reynolds number, covering strong, weak and neutral stratification; low, moderate and high background turbulence; and low and moderate Reynolds numbers. We observe a second vortex linking in a weakly stratified environment for the first time. The second vortex linking is followed by turbulence bursts that lead to the rapid decay of the residual vortices after the first vortex linking, leading to a short-living vortex pair. This challenges the conventional view that residual vortices have a long life span, which is true only in an unstratified environment. In addition to the second vortex linking, we observe the following. First, strong background turbulence quickly breaks the two vortices. Second, the two vortices induce secondary and tertiary vortices and lose energy to gravitational waves in a strongly stratified ($Fr \leqslant 0.7$) environment.

Key words: stratified flows

1. Introduction

The lift force on finite-span airplane wings produces a pair of counter-rotating trailing vortices in the wake as sketched in figure 1(*a*). These vortices persist for several minutes, translating to many miles behind the airplane. To avoid hazardous vortex encounters (McGowan 1968; Nelson 2004), the US Federal Aviation Administration has established

† Email address for correspondence: yxb5132@psu.edu

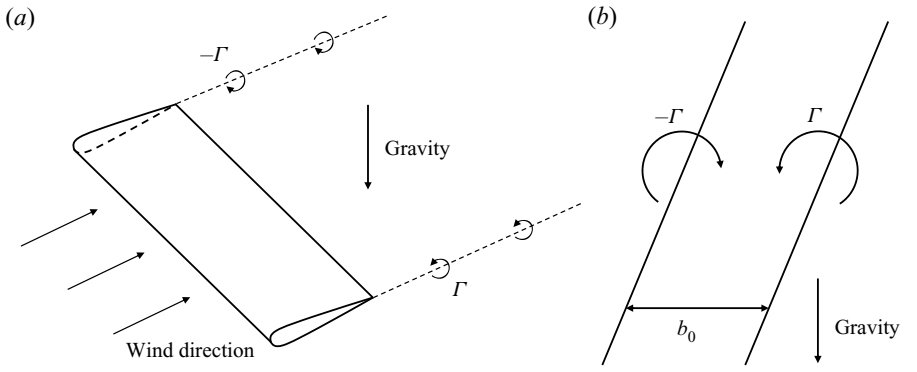

Figure 1. (*a*) A sketch of the counter-rotating vortices behind a finite-span airplane wing. (*b*) A sketch of counter-rotating vortices.

instrument flight rules that impose minimum separation distances for airplanes that land at the same airport, limiting airport capacity. In the above context, the rapid destruction of wake vortices is quite desirable. The same is true for the wake vortices behind submarines and stealth airplanes. These practical needs have motivated fundamental research of the wake vortex dynamics, and good reviews of the existing work can be found in Widnall (1975), Spalart (1998), Gerz, Holzäpfel & Darracq (2002) and Leweke, Le Dizès & Williamson (2016).

An extensively studied model problem is sketched in figure 1(*b*), where one neglects the effects of the ground and studies the decay or the collapse of a pair of counter-rotating vortices in a periodic domain. The vortices are assumed to be horizontal and perpendicular to the vertical direction, and, therefore, a zigzag instability (Billant 2010; Billant *et al.* 2010) does not play a role. The flow is controlled by the size of the vortex, d, the distance between the two vortices, b, the strength of the two vortices, Γ, and the fluid viscosity, ν. Two non-dimensional numbers can be identified, and they are the Reynolds number, $Re_\Gamma = \Gamma/\nu$, and the non-dimensional size of the vortex core, $d^* = d/b$. For most flows in the real world, the Reynolds number is high, and the size of the vortex core is much smaller than the distance between the two vortices. Hence, d^* is much smaller than 1, and Re_Γ is larger than 1 for practically relevant flows. There are three processes that are responsible for the destruction of the vortices: short-wave instability, long-wave instability or Crow instability/sinusoidal instability (Crow 1970), and viscous diffusion. Among the three processes, viscous diffusion is the least effective – although viscous effects are important during vortex linking and turbulence bursting. A short-wave instability, as the name suggests, is an instability at a wavelength (usually) smaller than the initial distance between the two vortices and does not involve any linking of the two primary vortices (Moore & Saffman 1975; Tsai & Widnall 1976). A short-wave instability leads to turbulence bursts within each vortex, and at practically relevant Reynolds numbers, the vortices would go through multiple cycles of short-wave instability before long-wave instability initiates (Leweke & Williamson 1998; Laporte & Corjon 2000) – if the vortices are not completely destroyed by the short-wave instability (McKeown *et al.* 2020). Note that when $d^* \ll 1$, the short-wave instability is very rare (Leweke *et al.* 2016). A long-wave instability (see figure 2) is an instability at a wavelength of the order of about 10 times the initial distance between the two vortices. The exact factor depending on d^*; see Crow (1970). A long-wave instability leads to vortex linking, which gives rise to vortex rings.

Ambient turbulence and (stable) vertical thermal stratification affect the aforementioned instabilities. The strength of vertical thermal stratification can be quantified by the Froude

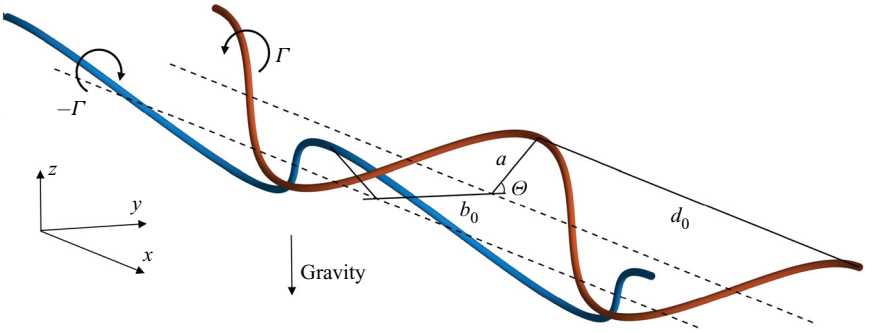

Figure 2. A sketch of the long-wave instability. Here d_0 is the wavelength, a is the amplitude, Θ is the inclination angle and b_0 is the initial distance between two vortices.

number, $Fr = W_0/(Nb_0)$, where N is the Brunt–Väisälä frequency and $W_0 = \Gamma/(2\pi b_0)$ is the induced velocity at the distance b_0. The strength of ambient turbulence can be quantified by the background turbulence intensity $\epsilon^* = (\epsilon b_0)/W_0$, where ϵ is the dissipation rate. Many have studied the effects of thermal stratification and ambient turbulence. In the following, we review the relevant work on long-wave instabilities. A basic theory of the long-wave instability is given by Crow (1970, 1974). Saffman (1972) and Crow & Bate (1976) built on Crow (1970)'s work and accounted for thermal stratification and ambient turbulence. Their work were further refined by Greene (1986), Klein, Majda & Damodaran (1995), Crouch (1997) and Switzer & Proctor (2002). These theories have been carefully scrutinized. Sarpkaya (1983) conducted experiments with three delta wings and two rectangular wings and investigated the decay of the trailing vortices in stratified and unstratified water. The author found first that thermal stratification reduces the lifespan of the trailing vortices and second that strong thermal stratification prevents vortex linking. van Jaarsveld *et al.* (2011) conducted a wind tunnel experiment and measured the decay of trailing vortices in a turbulent environment. The authors observed the short-wave instability, long-wave instability and vortices breakdown after the long-wave instability. The observed behaviour is in agreement with Crow & Bate (1976)'s theory, but the exact mechanism after the long-wave instability was not clear. Three-dimensional numerical simulations of the flow were not reported until about 2000. Before that, numerical simulations were mostly two dimensional (Hill 1975; Hecht, Bilanin & Hirsh 1981; Spalart 1996; Garten *et al.* 1998; Holzäpfel & Gerz 1999). While two-dimensional simulations give many insights into the descent of the trailing vortices, they cannot capture the long-wave instability. Lewellen & Lewellen (1996) and Lewellen *et al.* (1998) conducted three-dimensional large eddy simulations (LES) of aircraft wakes at conditions that mimic the realistic atmosphere. The long-wave instability leads to a series of vortex rings in their LES, which agree with the photographs taken from the ground. A lot more work is put into the model problem in figure 2. The simulation results show that weak thermal stratification accelerates vortex linking, and strong thermal stratification prevents the vortex linking (Robins & Delisi 1998; Holzäpfel, Gerz & Baumann 2001; Garten *et al.* 2001; De Visscher, Bricteux & Winckelmans 2013; Ortiz, Donnadieu & Chomaz 2015) – although the exact Froude number that demarcates weak stratification from strong stratification is left unspecified. The results also show that weak ambient turbulence accelerates vortex linking, and strong ambient turbulence rapidly destroys the vortices (Garten *et al.* 1998; Robins & Delisi 1998; Han *et al.* 2000*a*).

While the long-wave instability is fairly well understood, the collapse of the residual wake structure after the first vortex linking remains poorly understood for the following reasons. Firstly, visualizing and measuring the residual wake structures is non-trivial in a lab (Sarpkaya 1983; van Jaarsveld *et al.* 2011). Secondly, aside from a few direct numerical simulations (DNS) (Garten *et al.* 2001), most simulations are LES and rely on sub-grid scale models. Thirdly, except, for example, Misaka *et al.* (2012), most three-dimensional simulations stop shortly after long-wave instability completes.

The purpose of this work is to study the evolution of a pair of counter-rotating vortices in a stratified and turbulent environment during and, most importantly, after long-wave instability via DNS. We vary the Froude number from $Fr = 0.5$ to ∞ (unstratified), the ambient turbulence intensity from $\epsilon^* = 0.01$ to 1, and the Reynolds number from $Re_\Gamma = 942$ to 3768. We will show a second vortex linking in a weakly stratified environment followed by a rapid collapse of the residual vortices.

We distinguish this second vortex linking from the secondary vortex reconnections as described by van Rees, Hussain & Koumoutsakos (2012), Yao & Hussain (2020) and Hussain & Duraisamy (2011), which are results of high Reynolds numbers and can be observed in an unstratified environment. Specifically, the second vortex linking described here is the linking of the primary vortex ring and is a result of thermal stratification. The secondary vortex reconnections in Yao & Hussain (2020) (and various other previous works) manifest as turbulence bursts within the vortex tube (as evidenced in figure 7(*c*) in their paper) and are not a result of thermal stratification. In fact, the phenomenon described by Yao & Hussain (2020) has been found in many other studies with different initial conditions. In the following, we briefly review the literature. Direct numerical simulation studies of the reconnection process in an unstratified environment date back to Pumir & Kerr (1987), Kerr & Hussain (1989) and Shelley, Meiron & Orszag (1993). Melander & Hussain (1988, 1989) showed that the reconnection process has three stages, i.e. inviscid advection, bridging and threading. Saffman (1990) argued that the reconnection time scales vary logarithmically with Re_Γ. Other works on vortex reconnection can be found in Ji & Van Rees (2022), where the authors considered the bursting of a vortex tube due to the initial axial perturbation; Ostilla-Mónico *et al.* (2021), where the authors studied the collision of two vortex tubes at an angle; Pumir & Siggia (1990), where the authors simulated two anti-parallel vortex tubes to find the collapsing solution to the three-dimensional Euler equations; and Mishra, Pumir & Ostilla-Mónico (2021), where the authors considered the collision of two vortex rings. These previous studies all consider different set-ups. The reader is directed to the recent review by Yao & Hussain (2022) for a comprehensive review of the literature on vortex linking/reconnection.

The rest of the paper is organized as follows. The computational set-up is summarized in § 2, and we present the results in § 3. Conclusions are given in § 4.

2. Computational details

2.1. *Governing equations*

The flow is governed by the following Navier–Stokes equation with the Boussinesq approximation (Nomura *et al.* 2006):

$$\frac{\partial u_i}{\partial x_i} = 0, \tag{2.1}$$

$$\frac{\partial u_i}{\partial t} + u_j \frac{\partial u_i}{\partial x_j} = -\frac{1}{\rho_0}\frac{\partial p}{\partial x_i} + \nu \frac{\partial^2 u_i}{\partial x_j \partial x_j} + \alpha_T T g \delta_{i3}, \tag{2.2}$$

$$\frac{\partial T}{\partial t} + u_j \frac{\partial \left(\bar{T} + T\right)}{\partial x_j} = \kappa \frac{\partial^2 T}{\partial x_j \partial x_j}. \tag{2.3}$$

Equation (2.1) is the continuity, (2.2) is the momentum conservation and (2.3) is the transport equation of the temperature. Here u_i is the velocity in the ith Cartesian direction, x_i is the ith Cartesian direction, ρ_0 is the reference density, p is the deviation of the pressure from its hydrostatic value, ν is the kinematic viscosity, κ is the thermal diffusivity, g is the gravitational acceleration, $\bar{T}(z)$ is the imposed background temperature, $\partial\bar{T}/\partial t = 0$, $\partial^2\bar{T}/\partial z^2 = 0$, $\partial\bar{T}/\partial z = \text{const.}$ is the constant background temperature gradient, T is the temperature fluctuation, the instantaneous temperature is given by $\tilde{T} = T_0 + \bar{T}(z) + T$, T_0 is the reference temperature, δ_{ij} is the Kronecker delta, α_T is the volumetric expansion coefficient and is a constant, i.e. $\alpha_T \equiv -(1/\rho_0)(\partial\tilde{\rho}/\partial\tilde{T})$. The following length and velocity scale are used for normalization:

$$b_0, \quad W_0. \tag{2.4a,b}$$

Here b_0 is the distance between the two vortices at $t = 0$, W_0 is the advection velocity at a distance b from the vortex core at time $t = 0$ and Γ_0 is the circulation of one vortex at $t = 0$. The flow is controlled by the following three non-dimensional parameters, namely, the Reynolds number Re_Γ, the Froude number Fr and the background turbulence intensity ϵ^*. We consider two Reynolds numbers, i.e. $Re_{\Gamma,1} = 942$ and $Re_{\Gamma,2} = 3768$, five Froude numbers, i.e. $Fr = 0.5, 1, 2, 4$ and ∞, and four background turbulence intensities, i.e. $\epsilon^* = 0.01, 0.1, 0.25$ and 1. We vary the Froude number and the background turbulence intensity such that thermal stratification and background turbulence are significant at one end and insignificant at the other. Specifically, background turbulence is negligible when $\epsilon^* = 0.01$ and is dominant when $\epsilon^* = 1$; the flow is unstratified when $Fr = \infty$ and strongly stratified when $Fr = 0.5$. As for the Reynolds number, the results are, by and large, insensitive to the Reynolds number – at least in the range of the Reynolds numbers considered here. This is helpful because flows in the real world are at much higher Reynolds numbers.

2.2. *Initial condition*

The initial condition is a superposition of two flow fields, i.e. a forced homogeneous flow and two vortices. We specify the initial condition as follows. First, we compute a forced homogeneous flow at the desired Froude number in a periodic box. We follow De Visscher *et al.* (2013) and force the flow at the lowest two wavenumbers, i.e. $k_w = 2\pi/L_x$ and $k_w = 4\pi/L_x$. The forcing is adjusted until we get the ϵ^* we want. Figure 3 shows the normalized energy spectrum of the forced homogeneous turbulence. We see the familiar $-5/3$ scaling at the low wavenumbers – although the wavenumber range within which the energy spectrum follows the $-5/3$ scaling becomes narrower as ϵ^* decreases. This is expected: lower background turbulence requires forcing at a lower magnitude, which results in a lower Reynolds number and a narrower inertial range. Figure 4 shows contours of the x vorticity and temperature at a constant x location. We see more vigorous turbulence at higher ϵ^*. Specifically, we see barely any disturbance to the thermally stratified temperature fields in figure 4(*e*,*f*) for $\epsilon^* = 0.01$ and 0.10, but strong mixing of the low and high temperature fluid in figure 4(*h*) for $\epsilon^* = 1$. It is worth noting that we can see the oblique pattern in figure 4(*h*). Similar oblique patterns have been reported in the previous simulations, e.g. figure 5 in Chung & Matheou (2012) and figure 18 in Agrawal & Chandy (2021). However, we did not find an

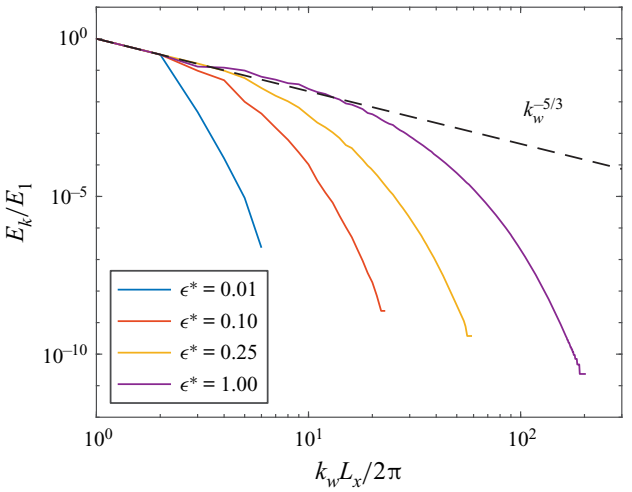

Figure 3. Energy spectra of the forced homogeneous flow in a stratified environment with $Fr = 2$ and $\epsilon^* = 0.01, 0.10, 0.25, 1.00$. The $-5/3$ law is plotted with a dashed line.

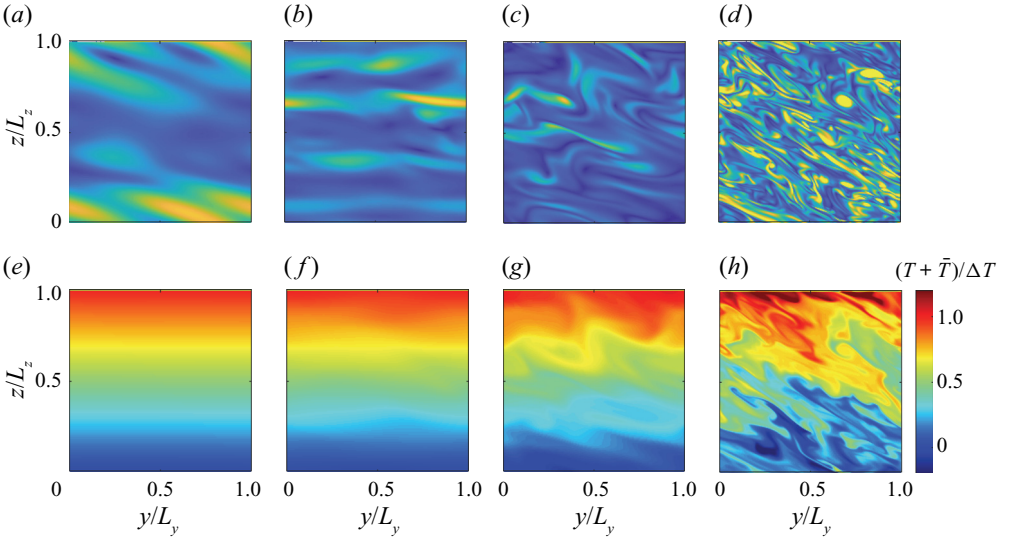

Figure 4. Contours of the x vorticity and temperature T in a constant x plane. The Froude number is $Fr = 2$. (*a–d*) Vorticity in the x-direction ω_x, here the contour levels are such that they encompass the maximum and minimum values in the domain; (*e–h*) $(T + \bar{T})/\Delta T$, where $\Delta T = L_z \, \mathrm{d}\bar{T}/\mathrm{d}z$ is the variation of the background temperature in the vertical domain. Results are shown for (*a,e*) $\epsilon^* = 0.01$, (*b,f*) $\epsilon^* = 0.10$, (*c,g*) $\epsilon^* = 0.25$, (*d,h*) $\epsilon^* = 1.00$.

explanation for this oblique pattern and will leave this interesting phenomenon to future investigation.

Next, we compute the flow field due to the two vortices. The locations of the vortex cores are given by

$$y_1(x) = y_{1,0} - a \sin(2\pi n x/L_x) \cos(\Theta), \tag{2.5}$$

$$z_1(x) = z_{1,0} + a \sin(2\pi n x/L_x) \sin(\Theta), \tag{2.6}$$

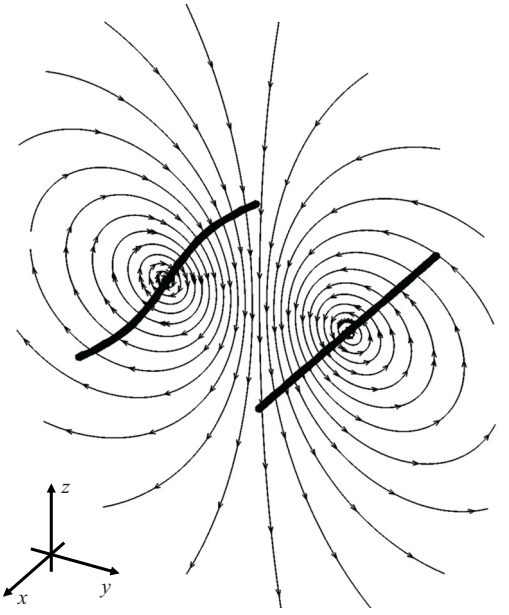

Figure 5. A visualization of the two vortices. The lines are stream lines at a constant x location through the mid-plane of the vortices.

$$y_2(x) = y_{2,0} + a\sin(2\pi nx/L_x)\cos(\Theta), \tag{2.7}$$

$$z_2(x) = z_{2,0} + a\sin(2\pi nx/L_x)\sin(\Theta), \tag{2.8}$$

where the subscripts 1 and 2 denote the first and second vortex, $y_{1,0}$, $z_{1,0}$, $y_{2,0}$ and $z_{2,0}$ are constants, and $y_{2,0} - y_{1,0} = b_0$, $z_{1,0} = z_{2,0}$. The second term adds perturbations to the otherwise straight vortices at the least stable wavenumber $k_w = 2\pi n/L_x = 2\pi/(8.6b_0)$ (Crow 1970). The amplitude of the perturbation is $a = 0.05b_0$, and the inclination angle is $\Theta = 48^\circ$ (Garten *et al.* 2001). The radius of the vortex core is $\sigma = 0.1b_0$, within which the vorticity magnitude is a constant $\omega_0 = \Gamma/(\pi\sigma^2)$. According to the Biot–Savart law, which is only used to construct the initial field, the two vortices give rise to the following vorticity field:

$$\omega_x(x, y, z, t = 0) = \omega_0(\mathrm{e}^{-\rho_1^2/\sigma^2} - \mathrm{e}^{-\rho_2^2/\sigma^2})\cos[a\cos(2\pi nx/L_x)], \tag{2.9}$$

$$\omega_y(x, y, z, t = 0) = -\omega_0(\mathrm{e}^{-\rho_1^2/\sigma^2} + \mathrm{e}^{-\rho_2^2/\sigma^2})\sin[a\cos(2\pi nx/L_x)]\cos(\Theta), \tag{2.10}$$

$$\omega_z(x, y, z, t = 0) = \omega_0(\mathrm{e}^{-\rho_1^2/\sigma^2} - \mathrm{e}^{-\rho_2^2/\sigma^2})\sin[a\cos(2\pi nx/L_x)]\sin(\Theta). \tag{2.11}$$

Here

$$\rho_i^2 = (y - y_i(x))^2 + (z - z_i(x))^2 \tag{2.12}$$

measures the distance from a generic location (x, y, z) to the ith vortex. Figure 5 is a visualization of the two vortices. The resulting velocity field can be obtained by solving the following Laplace equation:

$$\nabla^2\boldsymbol{u} = -\nabla\times\boldsymbol{\omega}. \tag{2.13}$$

The initial flow field is the superposition of the forced homogeneous turbulence and the two vortices. This way of obtaining the initial flow is similar to De Visscher *et al.* (2013).

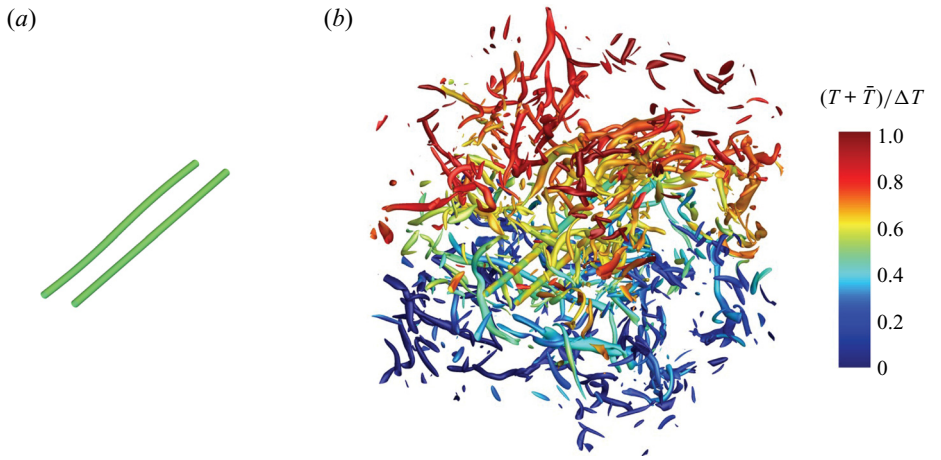

Figure 6. The Q isosurfaces, $Q^* = 1$, of the initial flow fields at (*a*) $\epsilon^\star = 0.01$ and (*b*) $\epsilon^\star = 1.00$. The isosurfaces are coloured by the $(\tilde{T} + \bar{T})/\Delta T$. The Froude number is $Fr = 2$ and the Reynolds number is $Re = 942$.

The two velocity fields are both divergence free, so it does not lead to any numerical difficulty, but whether the initial field is 'physical' is a question worth further investigation. Figure 6 shows the isosurfaces of $Q^* = 1$ of the initial vorticity at the condition $Re = 942$, $Fr = 2$ and $\epsilon^* = 0.01, 1.00$, where Q^* is defined as

$$Q^* = \frac{1}{2}(\omega^*_{ij}\omega^*_{ij} - S^*_{ij}S^*_{ij}), \quad \omega^*_{ij} = \frac{1}{2}\left(\frac{\partial u^*_i}{\partial x_j} - \frac{\partial u^*_j}{\partial x_i}\right), \quad S^*_{ij} = \frac{1}{2}\left(\frac{\partial u^*_i}{\partial x_j} + \frac{\partial u^*_j}{\partial x_i}\right), \tag{2.14a–c}$$

and $u^*_i \equiv u_i/\max(\sqrt{u^2_k})$ is the normalized velocity. The background turbulence level is low in figure 6(*a*), and the only visible vortical structures are the two counter-rotating vortices. On the other hand, in figure 6(*b*) the background turbulence level is high, and we see a lot more vortical structures than the two counter-rotating vortices.

2.3. *Further details*

Twenty-one DNS are conducted. The details of the DNS are tabulated in table 1. The nomenclature of the cases is as follows: Fr[Fr]E[ϵ^*]Re[L/M], where Fr is 0.5, 1, 2, or 4, ϵ^* is 0.01, 0.10, 0.25 and 1, L and M stand for low and moderate. There are four groups of DNS. In the first group, we vary the Froude number whilst keeping the background turbulence negligible. The purpose is to study the effects of thermal stratification. In the second group, we vary the background turbulence intensity whilst keeping thermal stratification negligible. The purpose is to study the effects of background turbulence. In the third group, we vary the turbulence intensity whilst keeping $Fr = 2$. The purpose is to study the effects of both the background turbulence and thermal stratification. Last, in the fourth group, we vary the Reynolds number. The purpose is to show that our results are insensitive to the Reynolds number.

The computational domain is a periodic box. Except for Fr2.0E0.01ReM, for which the domain size is $L_x \times L_y \times L_z = 8.6b_0 \times 12.9b_0 \times 8.6b_0$, we employ a domain of size $L_x \times L_y \times L_z = 8.6b_0 \times 8.6b_0 \times 8.6b_0$. The grid spacing is uniform in all three directions, and the resolution is slightly finer than that in Garten *et al.* (2001). We ensure that the

Group	Case name	Re_Γ	Fr	Pr	$\epsilon^\star$	L_x/b_0	L_y/b_0	L_z/b_0	N_x	N_y	N_z	σ/Δ_y
1/3/4	Fr0.5E0.01ReL	942	0.5	1	0.01	8.6	8.6	8.6	432	432	432	5.0
1	Fr0.6E0.01ReL	942	0.6	1	0.01	8.6	8.6	8.6	432	432	432	5.0
1	Fr0.7E0.01ReL	942	0.7	1	0.01	8.6	8.6	8.6	432	432	432	5.0
1	Fr0.8E0.01ReL	942	0.8	1	0.01	8.6	8.6	8.6	432	432	432	5.0
1	Fr0.9E0.01ReL	942	0.9	1	0.01	8.6	8.6	8.6	432	432	432	5.0
1	Fr1.0E0.01ReL	942	1.0	1	0.01	8.6	8.6	8.6	432	432	432	5.0
1	Fr2.0E0.01ReL	942	2.0	1	0.01	8.6	8.6	8.6	432	432	432	5.0
1	Fr4.0E0.01ReL	942	4.0	1	0.01	8.6	8.6	8.6	432	432	432	5.0
1	Fr6.0E0.01ReL	942	6.0	1	0.01	8.6	8.6	8.6	432	432	432	5.0
1	Fr8.0E0.01ReL	942	8.0	1	0.01	8.6	8.6	8.6	432	432	432	5.0
1	Fr10.0E0.01ReL	942	10.0	1	0.01	8.6	8.6	8.6	432	432	432	5.0
1	Fr100.0E0.01ReL	942	100.0	1	0.01	8.6	8.6	8.6	432	432	432	5.0
1/2	FrInfE0.01ReL	942	∞	1	0.01	8.6	8.6	8.6	432	432	432	5.0
2	FrInfE0.00ReL	942	∞	1	0.00	8.6	8.6	8.6	432	432	432	5.0
2	FrInfE0.10ReL	942	∞	1	0.10	8.6	8.6	8.6	432	432	432	5.0
2	FrInfE0.25ReL	942	∞	1	0.25	8.6	8.6	8.6	432	432	432	5.0
2	FrInfE1.00ReL	942	∞	1	1.00	8.6	8.6	8.6	432	432	432	5.0
3	Fr2.0E0.10ReL	942	2.0	1	0.10	8.6	8.6	8.6	432	432	432	5.0
3	Fr2.0E0.25ReL	942	2.0	1	0.25	8.6	8.6	8.6	432	432	432	5.0
3	Fr2.0E1.00ReL	942	2.0	1	1.00	8.6	8.6	8.6	432	432	432	5.0
4	Fr2.0E0.01ReM	3768	2.0	1	1.00	8.6	12.9	8.6	1152	1728	1152	14.4

Table 1. Direct numerical simulation details.

grid is sufficiently fine for the high ϵ^* cases and apply that grid to the low ϵ^* cases. Specifically, the grid resolution is $\Delta/\eta \leqslant 0.85$ in all DNS, where η is the Kolmogorov length scale. The time step size is such that CFL $= 0.6$.

The in-house finite-difference code AFiD is employed for the DNS. The code is second order in space and uses the third-order Runge–Kutta scheme in time.

Further details of the numerics can be found in Ostilla-Monico *et al.* (2015), van der Poel *et al.* (2015) and Kim & Moin (1985). The code has been extensively used for stratified flows (Yang *et al.* 2015, 2020; Du, Zhang & Yang 2021; Li & Yang 2021), and we present a validation in Appendix A.

3. Result

3.1. *Basic phenomenology*

Figure 7 visualizes the evolution of the vortex pair in case Fr2.0E0.01ReM. First, the two vortices get close to each other as a result of the Crow instability. Meanwhile, they move downward as a result of induced velocity. This is shown in figure 7(*a*). The dissipation is about uniform in each vortex until the two vortex link, which happens at $t^* = 3$, where t^* is normalized time and defined as

$$t^* \equiv tW_0/b_0. \tag{3.1}$$

This is the first vortex linking, and it gives rise to a vortex ring. Large dissipation is found at the location where the two vortices link, as shown in figure 7(*b*). The first vortex linking marks the completion of sinusoidal instability. This process is very well understood (Crow

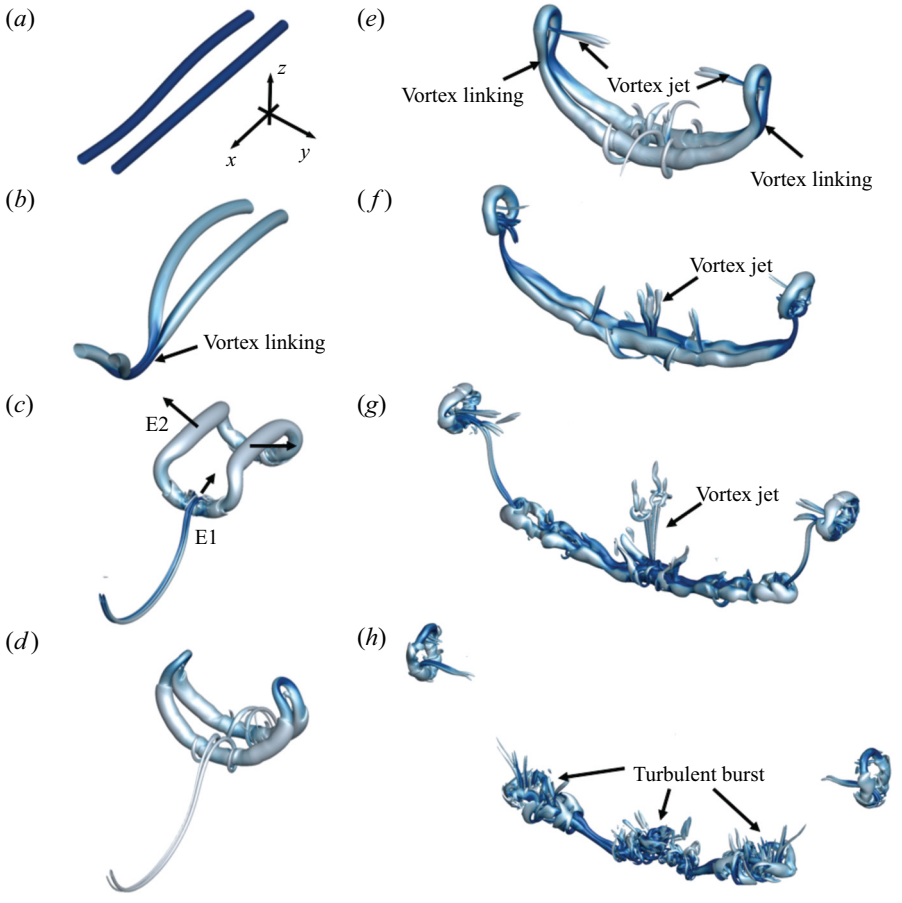

Figure 7. Isosurface of $Q^* = 1$ at $t^* = 1$, 3, 4, 5, 5.5, 6, 6.5 and 7.0 for case Fr2.0E0.01ReM. The isosurfaces are coloured by viscous dissipation. Light blue indicates low dissipation, and dark blue indicates high dissipation.

1970), and we leave the discussion brief. The focus of this study is the decay of the residual vorticity after the first vortex linking, which is still poorly understood.

After the first vortex linking, the vertical position of the two vortices do not change significantly until the second vortex linking at $t^* = 5.5$. Between the first and second vortex linking, the size of the vortex ring collapse in the longitudinal (y) direction. Specifically, among the four ends of the vortex ring, the distance between E1 and its opposite end decreases, whereas the distance between E2 and its opposite end increases, as shown in figure 7(c). This process continues, leading to two wrapped semicircle-shaped vortices in figure 7(d), followed by the second vortex linking at two locations in figure 7(e). The second vortex linking gives rise to two small vortex rings and two line vortices. The evolution of these residual vortices is shown in figure 7(f,g,h). The two small vortex rings travel left and right and leave. The two line vortices collide, leading to rapid vortex decay. In the process, we see a few weak vortex jets, which quickly dissipate. We also see turbulence bursts, which lead to the demise of the residual vortices.

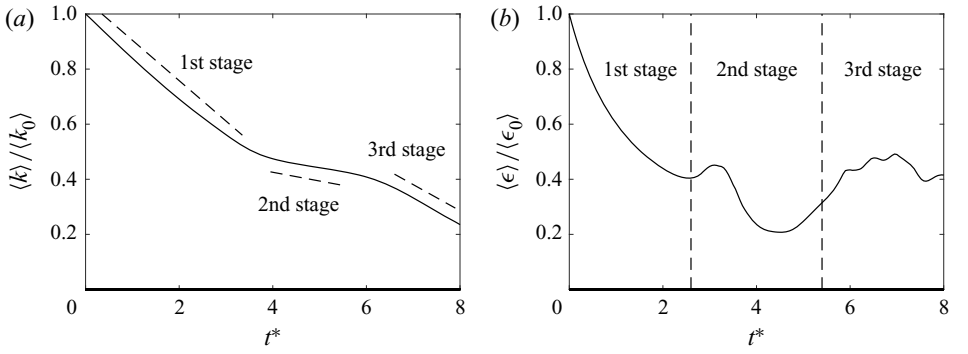

Figure 8. The volume integrated (*a*) kinetic energy $\langle k \rangle$ and (*b*) dissipation term $\langle \epsilon \rangle$ as a function of the non-dimensional time t^*. Here, k_0 and ϵ_0 are the kinetic energy and viscous dissipation at $t^* = 0$.

To quantify the physics that is responsible for the decay of the vortices, we turn to the following kinetic energy equation:

$$\frac{\partial k}{\partial t} + \frac{\partial (u_i k)}{\partial x_i} = -\frac{1}{\rho_0}\frac{\partial (u_i p)}{\partial x_i} + \nu \frac{\partial^2 k}{\partial x_i^2} - \epsilon + P_g. \tag{3.2}$$

Here the kinetic energy k is

$$k \equiv \frac{u_i u_i}{2}, \tag{3.3}$$

the dissipation term ϵ is

$$\epsilon \equiv \nu \frac{\partial u_i}{\partial x_j}\frac{\partial u_i}{\partial x_j} \tag{3.4}$$

and the gravitational term P_g is

$$P_g \equiv \alpha_T T g u_3. \tag{3.5}$$

The gravitational term represents the exchange between the gravitational potential energy and kinetic energy. The dissipation term ϵ destroys kinetic energy. Figure 8 shows the domain integrated k and ϵ as a function of time. We see three distinct stages in figure 8(*a*): the flow loses energy quickly from $t^* = 0$ to $t^* = 2.6$, i.e. before the first vortex linking, barely loses any kinetic energy from $t^* = 2.6$ to $t^* = 5.4$, i.e. between the first and the second vortex linking, and quickly loses energy beyond $t^* = 5.4$, i.e. after the second vortex linking and during the bursts. Figure 8(*b*) shows a similar trend: the dissipation rate dips between $t^* = 2.6$ and $t^* = 5.4$, i.e. between the first and the second vortex linking.

Tools like Q isosurfaces and time histories of volume integrated kinetic energy and viscous dissipation have been extensively used in previous studies (Han *et al.* 2000*b*; Moet *et al.* 2000; Holzäpfel *et al.* 2003; Nomura *et al.* 2006; Misaka *et al.* 2012). The Q isosurfaces contain spatial information, but they lack temporal information. Time histories of volume integrated kinetic energy and viscous dissipation have temporal information, but they lack spatial information. In a lot of previous work (Garten *et al.* 2001; De Visscher *et al.* 2013), Q isosurfaces and time histories of volume integrated kinetic energy and viscous dissipation are shown together to complement each other. However, it would be rather cumbersome to show Q isosurfaces and time histories of k and ϵ for all DNS cases. We need a tool that contains both temporal information and spatial information. In search of such a tool, we find that the transverse (y and z directions) integrated turbulent kinetic

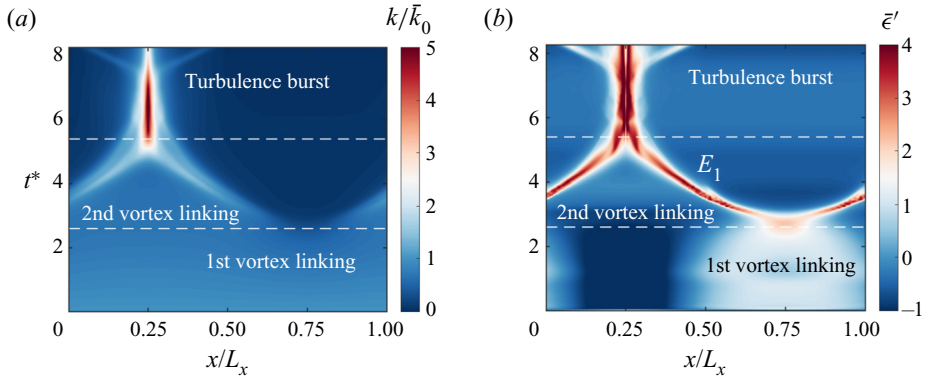

Figure 9. (*a*) Contour of the transverse averaged kinetic energy $\bar{k}$ as a function of the x coordinate and time. (*b*) Same as (*a*) but for $\bar{\epsilon}'$.

energy and viscous dissipation, i.e. $\bar{k}$ and $\bar{\epsilon}$, are good candidates. Figure 9 shows $\bar{k}$ and $\bar{\epsilon}'$ as a function of time, where

$$\bar{\epsilon}' = \frac{\bar{\epsilon} - \langle\epsilon\rangle}{\mathrm{STD}(\bar{\epsilon} - \langle\epsilon\rangle)}, \tag{3.6}$$

and STD$(\cdot)$ is the standard deviation of the variable in the parentheses. We see first and second vortex linking at $x/L_x = 0.75$, $t^* = 2.6$ and $x/L_x = 0.25$, $t^* = 5.4$, as well as turbulence bursts. We also see the rapid decay of the kinetic energy and the surge of viscous dissipation after the second vortex linking. Note that $\bar{k}$ and $\bar{\epsilon}'$ carry similar information. In the following subsections we will use the transverse averaged viscous dissipation and only show Q isosurfaces and time histories of volume-averaged kinetic energy and dissipation rate when necessary.

3.2. *The second vortex linking*

We observe a second vortex linking followed by turbulence bursts and the rapid decay of the residual vortices. This directly contradicts the findings in Misaka *et al.* (2012), where the residual vortices after the first vortex linking are found to persist for a long time. In this subsection we will explain this difference.

Misaka *et al.* (2012) and this work differ in the following. Firstly, Misaka *et al.* (2012) is an LES study, and the authors considered a higher Reynolds number. Secondly, Misaka *et al.* (2012) considered vortex evolution in an unstratified environment. It is critical that we understand what is responsible for the long life span of the residual vortices in Misaka *et al.* (2012). Note that we do not doubt the reliability of LES results from Misaka *et al.* (2012). In fact, a similar long-living vortex ring is reported by other researchers, e.g. Leweke & Williamson (2011). Our unstratified case, i.e. FrInfE0.01ReL, also shows a long-living vortex ring, as demonstrated in figure 11, Thus, we think it is hard to argue that LES is responsible for the difference in life span.

Figure 10(*a*) shows $\bar{\epsilon}'$ in case Fr2.0E0.01ReL. Case Fr2.0E0.01ReL is at the same condition as case Fr2.0E0.01ReM except that case Fr2.0E0.01ReL is at a lower Reynolds number. We see the first vortex linking at $x/L_x = 0.75$, $t^* = 3.5$, the second vortex linking at $x/L_x = 0.25$, $t^* = 7$, and the subsequent turbulence bursts; this is similar to figure 9(*b*). Figure 10(*b*,*c*) shows the Q isosurfaces at $t^* = 7$ and 9. We see turbulence bursts as in figure 7(*h*). However, because the flow is at a lower Reynolds number than

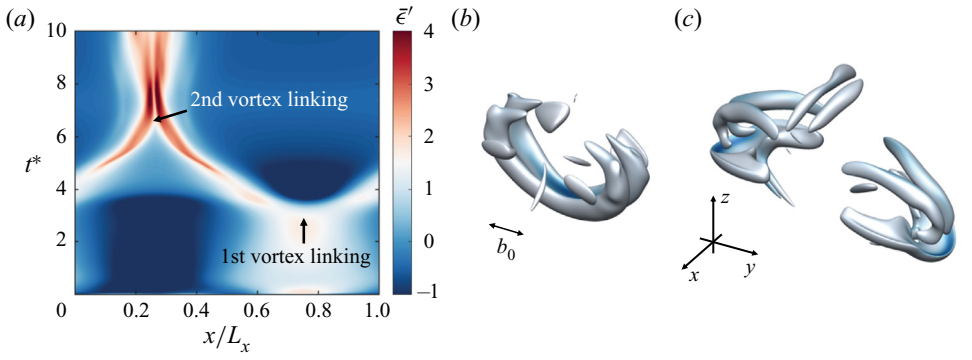

Figure 10. (*a*) Same as figure 9(*b*) but for case Fr2.0E0.01ReL. Isosurface of $Q^* = 0.6$ at (*b*) $t^* = 7$ and (*c*) $t^* = 9$.

Fr2.0E0.01ReM, we see only one bulb of eddies and fewer structures in figure 10 than in figure 7(*h*). Hence, the Reynolds number cannot explain the difference between Misaka *et al.* (2012) and the present work. Figure 11 shows the transverse averaged dissipation rate $\bar{\epsilon}'$ in case FrInfE0.01ReL. Case FrInfE0.01ReL is at the same condition as Fr2.0E0.01ReL except that FrInfE0.01ReL is unstratified. We see the first vortex linking at $t^* = 4$. Figures 11(*b*,*c*,*d*) show the Q isosurfaces at $t^* = 10$, 20 and 30. We do not see second vortex linking nor turbulence bursts. Instead, the vortex ring oscillates and persists for a long time. Hence, we conclude that the unstratified environment is responsible for the long life span of the residual vortices in Misaka *et al.* (2012). In other words, the stratified environment causes the second vortex linking.

Next, we interrogate the DNS for the flow structures that are responsible for the second vortex linking in a stratified environment. Figure 12(*a*) shows the contour of the y-direction vorticity ω_y at $y = 0.5(L_y + b_0)$, $t^* = 5$ in Fr2.0E0.01ReM, which is slightly off centre and at a time before the second vortex linking. The centres of the primary vortices are at $(x, z) = (0.17L_x, 0.44L_z)$ and $(x, z) = (0.33L_x, 0.44L_z)$. The primary vortices induce secondary vortices, as indicated in figure 12(*a*). We may roughly divide the secondary vortices into the upper part and the lower part, whose z coordinates are above and below that of the primary vortices. We see that the upper part is stronger than the lower part. Consequently, the secondary vortices induce a velocity that pushes the left primary vortex to the right and the right primary vortex to the left. This eventually leads to the second vortex linking, as we see in figure 7(*e–f*). This is consistent with the previous studies, where the distance between two counter-rotating vortices decreases in a stratified environment (Saffman 1972; Spalart 1996; Garten *et al.* 1998; Ortiz *et al.* 2015). Figure 12(*b*) shows y vortices in Fr2.0E0.01ReL before the second vortex linking. We see, again, the secondary vortices, which have a comparably stronger upper part and a comparably weaker lower part. Lastly, figure 12(*c*) shows the contours of the y vortices in FrInfE0.01ReL after the first vortex linking. This case does not give rise to a second vortex linking, and in figure 12(*c*) we see no secondary vortices. In all, we conclude that the second vortex linking is a consequence of the secondary vortices, which are due to flow stratification.

The generation of the secondary vortices can be attributed to the P_g term in (3.2). In figure 13 we examine the behaviour of the term P_g. Figure 13(*a*) shows the evolution of the volume integrated P_g in the Fr2.0E0.01ReL case. It first decreases, then increases and finally decreases again. Figure 13(*b*,*c*) shows the contours of P_g before the first and second

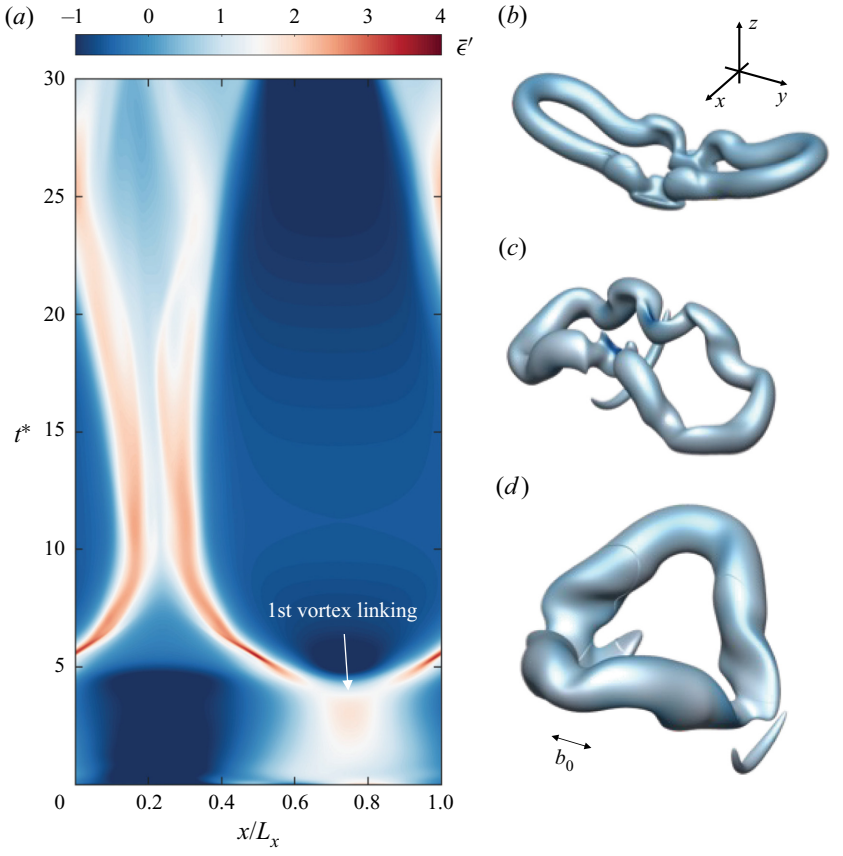

Figure 11. (*a*) Same as figure 9(*b*) but for case FrInfE0.01ReL. Isosurface of $Q^* = 0.6$ at (*b*) $t^* = 10$, (*c*) $t^* = 20$ and (*d*) $t^* = 30$.

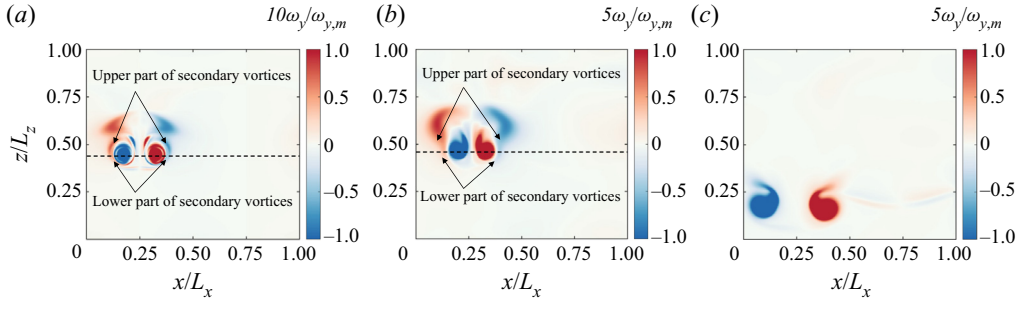

Figure 12. Contours of the *y*-direction vorticity ω_y on $y = 0.5(L_y + b_0)$ plane for (*a*) case Fr2.0E0.01ReM at $t^* = 5$, (*b*) case Fr2.0E0.01ReL at $t^* = 6$ and (*c*) case FrInfE0.01ReL at $t^* = 7$. To show secondary vortices clearly, the contours are respectively normalized by (*a*) $0.1\omega_{y,m}$, (*b*) $0.2\omega_{y,m}$ and (*c*) $0.2\omega_{y,m}$. Here, $\omega_{y,m}$ is the maximum *y*-direction vorticity on each plane.

vortex linking at a constant *x*. We see that the term is negative between the two primary vortices (the locations of the two primary vortices are indicated using two arrows) and positive on the outer sides of the vortices, which subsequently leads to the secondary vortices (as shown in figure 12*a*).

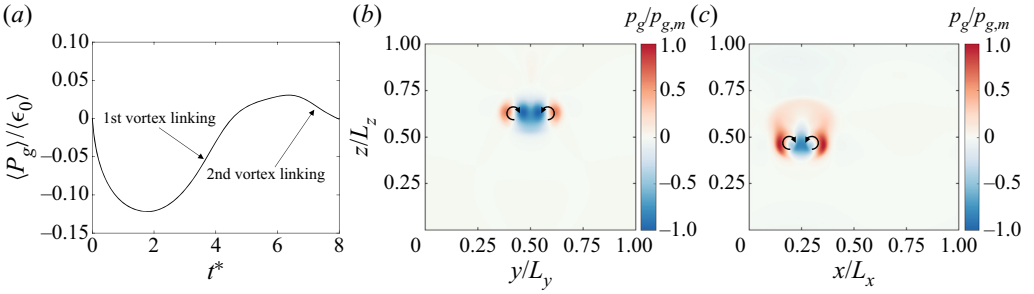

Figure 13. (*a*) The volume integrated gravitational term $\langle P_g \rangle$ as a function of t^*, where $\langle \epsilon_0 \rangle$ is the volume integrated initial dissipation. (*b*) Contour of P_g at $t^* = 3$, $x = 0.75L_x$. (*c*) Contour of P_g at $t^* = 6$, $y = 0.5(L_y + b_0)$ in case Fr2.0E0.01ReL. Here $P_{g,m}$ is the maximum value of P_g in the plane, and arrows indicate the location of the primary vortices.

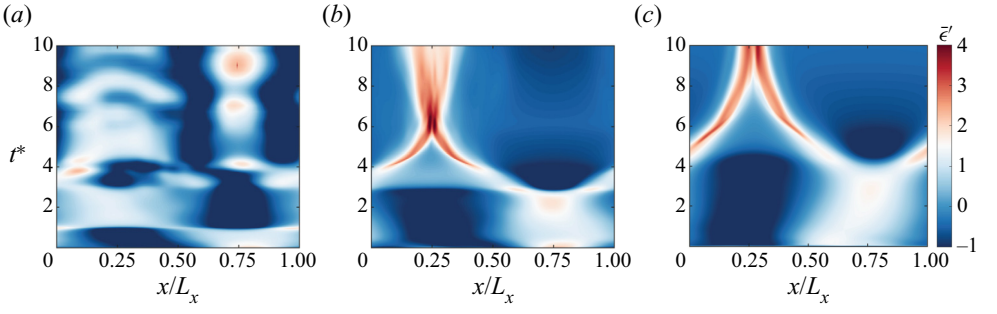

Figure 14. Transverse averaged dissipation $\bar{\epsilon}'$ in case (*a*) Fr0.5E0.01ReL, (*b*) Fr1.0E0.01ReL, (*c*) Fr4.0E0.01ReL.

In the next few subsections we discuss the impacts of stratification and background turbulence. Again, the discussion will focus on the evolution of the vortices after the first vortex linking (at large t^*).

3.3. *Thermal stratification and background turbulence*

First, we vary the Froude number from 0.5 to ∞ whilst keeping the Reynolds number $Re_\Gamma = 942$ and $\epsilon^* = 0.01$ constant. The background turbulence is negligibly weak and insignificant. As we will show, the flow is strongly stratified when $Fr \leqslant 0.7$, weakly stratified when $Fr > 0.7$, and unstratified conditions when $Fr = \infty$.

Figure 14 shows the transverse averaged dissipation $\bar{\epsilon}'$ as a function of both x and t^* for $Fr = 0.5$, 1 and 4. The $Fr = 2$ result is shown in figure 10(*a*) and the $Fr = \infty$ result is shown in figure 11(*a*). The $Fr = 1$, 2, 4 results are qualitatively similar. The first vortex linking occurs at $t^* = 3.7$, 3.5, 3.0 and 2.5 for $Fr = \infty$, 4, 2 and 1, respectively. The second vortex linking occurs at $t^* = 8.3$, 6.5 and 5.2 for Fr =4, 2 and 1, respectively, and the time it takes for the vortices to link a second time decreases as the Froude number decreases (as stratification becomes stronger). There is no second vortex linking when $Fr = \infty$. The $Fr = 0.5$ result is qualitatively different from the rest, and we see no vortex linking at all. These results are consistent with those in Garten *et al.* (1998, 2001), and Sarpkaya (1983): thermal stratification accelerates sinusoidal instability until strong stratification prevents sinusoidal instability completely. These results are also consistent with the results in § 3.1: a second vortex linking occurs in a weakly stratified environment.

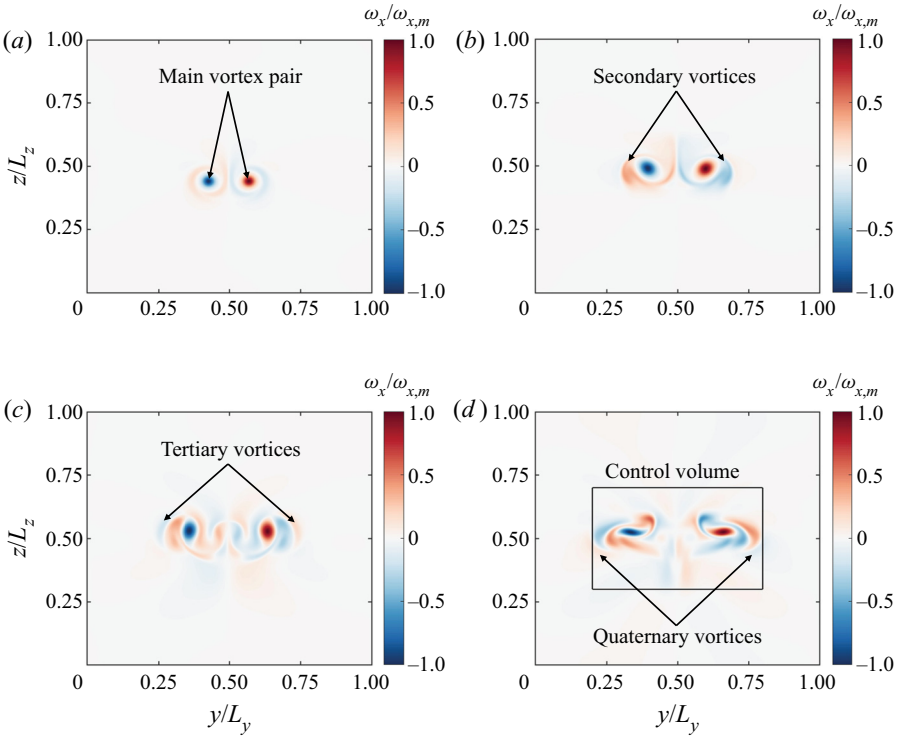

Figure 15. Contour of normalized x-direction vorticity $\omega_x/\omega_{x,m}$ at $x = 0.5L_x$, (*a*) $t^* = 1$, (*b*) $t^* = 2$, (*c*) $t^* = 3$, (*d*) $t^* = 4$. Here $\omega_{x,m}$ is the maximum value of ω_x.

In case Fr0.5E0.01ReL vortex linking is prevented completely. To get some insights into the flow dynamics, figure 15 shows the contour of the x-direction vorticity ω_x. We see gravitational waves in (*b–d*). The vortex pair gives rise to secondary vortices, which, in turn, give rise to tertiary vortices and quaternary vortices. This process would continue indefinitely until the gravitational waves drain the kinetic energy in the vortex pair.

Quantitatively speaking, the energy loss due to gravitational waves can be obtained by computing the energy flux at the surface of a control volume that encompasses the primary vortices. We define the control volume as in figure 15(*d*). It is a rectangular box and encompasses $y/L_y \in [0.2, 0.8]$, $z/L_z \in [0.3, 0.7]$. The flux due to pressure waves is given by

$$F_p \equiv \oint_V \frac{p\boldsymbol{u}}{\rho_0} \cdot \boldsymbol{n}\, \mathrm{d}S, \tag{3.7}$$

where $\boldsymbol{n}$ is the normal vector pointing from the inside of the control volume to the outside. Thus, positive F_p corresponds to the energy loss. We normalize F_p^* with W_0 and b_0 like other quantities. Figure 16 shows F_p^* as a function of t^*. We see that F_p^* is positive shortly after the initial transient period, and, thus, the primary vortices keep losing energy to internal gravitational waves.

A question we could ask is how stratification generates secondary vortices in a strongly stratified environment. The governing equation for vorticity is

$$\frac{\partial \omega_i}{\partial t} + u_j \frac{\partial \omega_i}{\partial x_j} - \omega_j \frac{\partial u_i}{\partial x_j} = \nu \frac{\partial^2 \omega_i}{\partial x_j^2} + \alpha_T g \left(\delta_{1i} \frac{\partial T}{\partial y} - \delta_{2i} \frac{\partial T}{\partial x} \right), \tag{3.8}$$

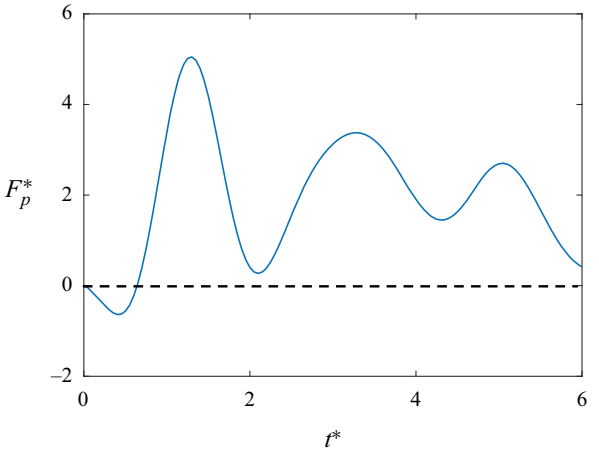

Figure 16. The flux of the pressure term F_p^* on the control volume as the function of t^*.

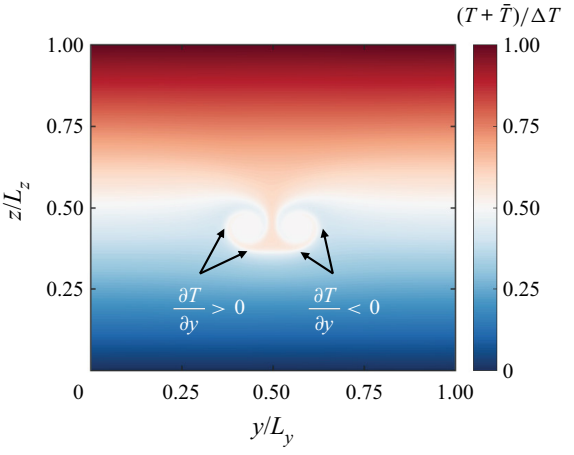

Figure 17. Contour of the normalized temperature $(T+\bar{T})/\Delta T$ at the same x/L_x and t^* as figure 15(*a*).

where the last term shows that stratification generates vorticity. Figure 17 shows the contour of the normalized temperature at the same x location and time t^* as figure 15(*a*). The primary vortex pair brings the lighter fluid among the heavier fluid. In these regions, $\partial T/\partial y \neq 0$, and vortices are generated as a result. This process, of course, will not happen in unstratified flows.

Having discussed the effects of thermal stratification, next, we vary the background turbulence level from $\epsilon^* = 0.01$ to 1.0 whilst keeping the Froude number at $Fr = \infty$ and the Reynolds number at $Re_\Gamma = 942$. The background turbulence is weak when $\epsilon^* = 0.01$ and 0.1 and strong when $\epsilon^* = 0.25$ and 1. Recall that the vortex ring, which directly results from the first vortex linking, persists for a long time in the absence of background turbulence. In the following, we examine the impact of background turbulence on the vortex ring.

Figure 18 shows the time histories of the volume integrated kinetic energy and viscous dissipation. We normalize the kinetic energy and the viscous dissipation by their values at $t^* = 0$ in case FrInfE0.01ReL. The background turbulence contributes to the kinetic

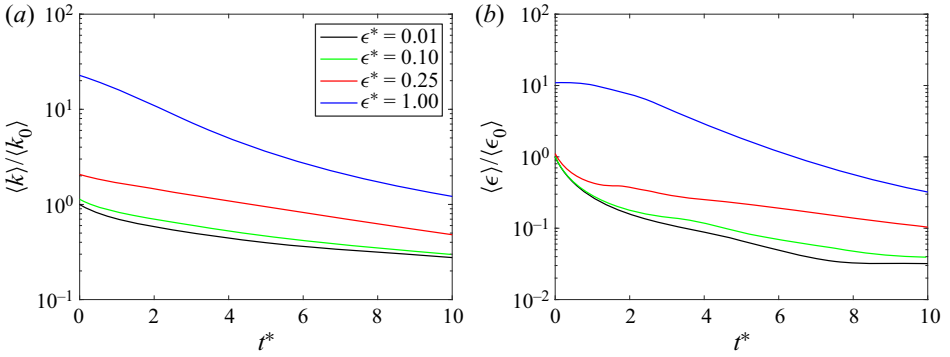

Figure 18. The volume integrated (*a*) kinetic energy and (*b*) viscous dissipation as a function of time, where $\langle k_0 \rangle$ and $\langle \epsilon_0 \rangle$ is the initial volume integrated value in the FrInfE0.01ReL case.

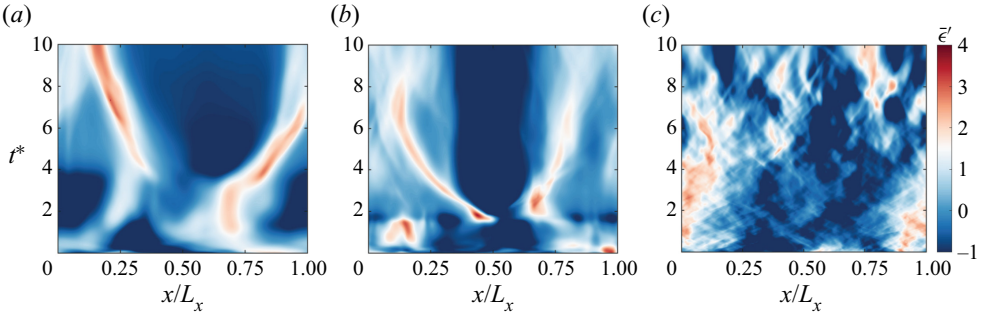

Figure 19. Transverse integrated dissipation $\bar{\epsilon}'$ in case (*a*) FrInfE0.10ReL, (*b*) FrInfE0.25ReL and (*c*) FrInfE1.00ReL.

energy and the dissipation: at $t^* = 0$, the normalized kinetic energy is 22.5, 2.06, 1.14 in cases FrInfE0.10ReL, FrInfE0.25ReL and FrInfE1.00ReL, and the normalized dissipation is 11, 1.114, 1.007. When the background turbulence is strong, the vortex pair is a lesser part of the flow. It should follow that the flow is less controlled by the vortex dynamics in the presence of strong background turbulence. This is not immediately clear from figure 18: in all cases, the kinetic energy and the dissipation decay as a function of time. To get some insights into the flow dynamics, we examine the transverse averaged viscous dissipation.

Figure 19 shows the transverse averaged dissipation $\bar{\epsilon}'$. The FrInfE0.01ReL result is shown in figure 11(*a*). Background turbulence disturbs the flow. The $\epsilon^* = 0.10$ and 0.25 results in (*a*,*b*) look qualitatively similar to the $\epsilon^* = 0.01$ result in figure 11(*a*). We see the first vortex linking at $t^* = 3.3, x/L_x = 0.57$ and $t^* = 1.5, x/L_x = 0.55$, respectively, but no second vortex linking. Nonetheless, the vortex ring (a result of the first vortex linking) does not necessarily persist for a long time. In case FrInfE1.00ReL the background turbulence is so strong that it tore the vortex pair quickly, as we can see in (*c*). To see what is happening in the flow when there is strong background turbulence, we visualize the vortices in case FrInfE1.00ReL in figure 20. We see that the background turbulence quickly dissipates the vortex pair, and at $t^* = 2$ we can no longer find the vortex pair.

So far, we varied the Froude number in a flow where there is essentially no background turbulence. We also varied the background turbulence level in a flow with no stratification. Now, we consider a flow with both thermal stratification and background turbulence. Specifically, we vary the background turbulence intensity from $\epsilon^* = 0.01$ to 1.0 whilst

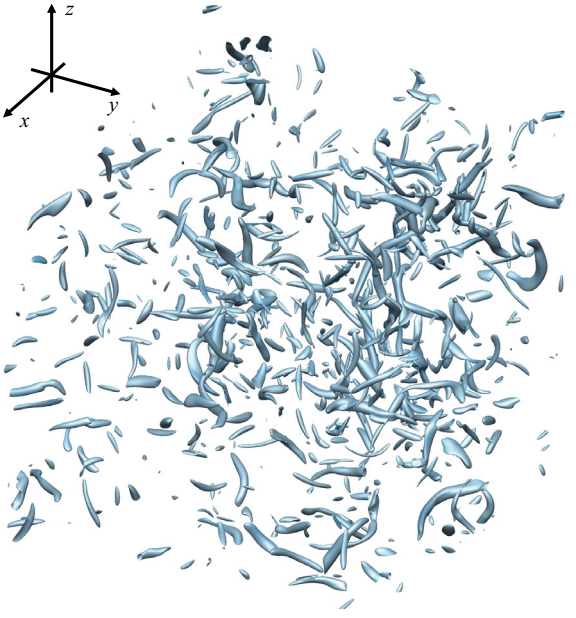

Figure 20. Isosurface of $Q^* = 5$ for the FrInfE1.00ReL case at $t^* = 2$.

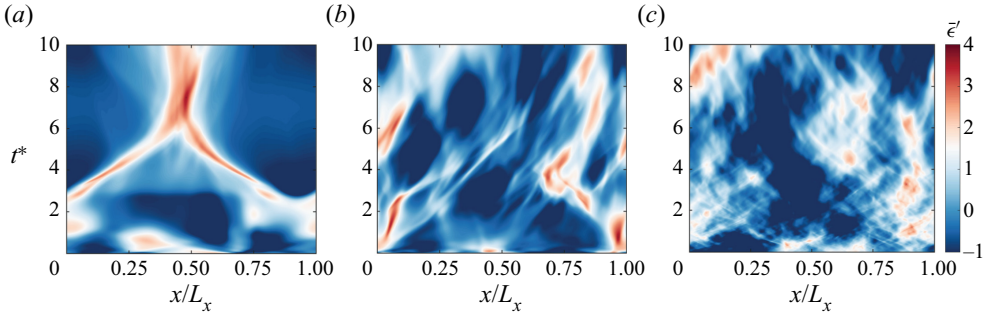

Figure 21. Transverse averaged dissipation $\bar{\epsilon}'$ in case (*a*) Fr2.0E0.10ReL, (*b*) Fr2.0E0.25ReL and (*c*) Fr2.0E1.00ReL.

keeping $Fr = 2.0$ and $Re_\Gamma = 942$. The objective is to see if there is any nonlinear interplay between thermal stratification and background turbulence.

Figure 21 shows the transverse averaged dissipation $\bar{\epsilon}'$ in cases Fr2.0E0.10ReL, Fr2.0E0.25ReL and Fr2.0E1.00ReL. The Fr2.0E0.01ReL results are shown in figure 10. When the background turbulence is at a low level, i.e. $\epsilon^* = 0.10$, there is a second vortex linking and subsequent turbulence bursts. However, when the background turbulence is at a high level, i.e. $\epsilon^* = 0.25$, 1.00, the two vortices rapidly dissipate, and there is no second vortex linking. In all, we do not see any apparent nonlinear interplay between thermal stratification and background turbulence: thermal stratification plays the dominant role when the background turbulence level is low, and background turbulence plays the dominant role when it is strong.

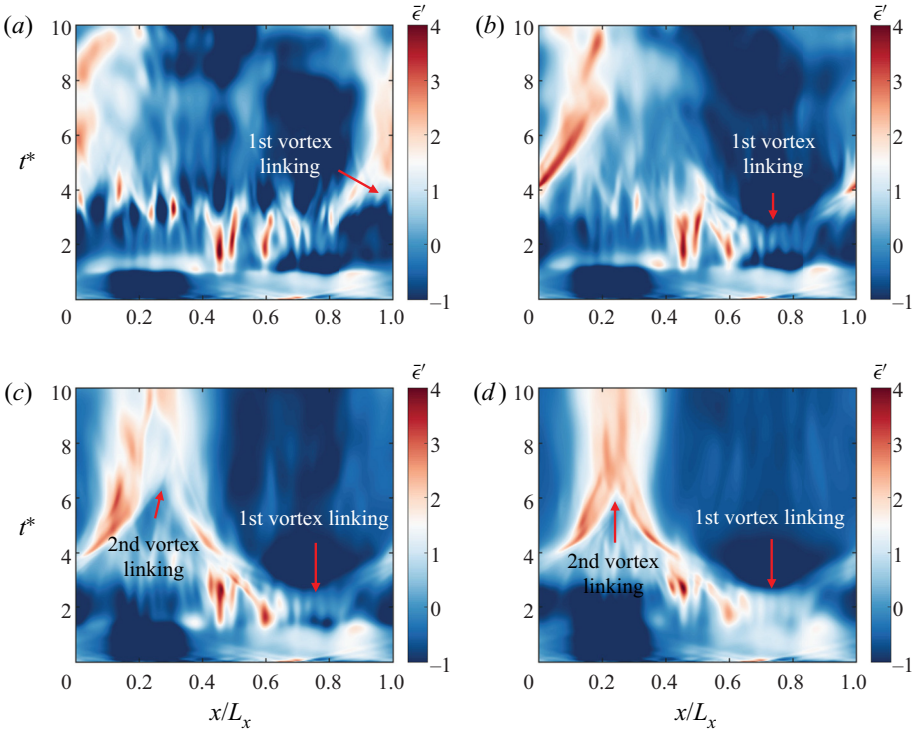

Figure 22. Contour of $\bar{\epsilon}'$ as a function of the x coordinate and the time for case (*a*) Fr0.6E0.01ReL, (*b*) Fr0.7E0.01ReL, (*c*) Fr0.8E0.01ReL, (*d*) Fr0.9E0.01ReL.

3.4. *Critical Froude number*

The second vortex linking can be observed in a weakly stratified environment but not in a strongly stratified and unstratified environment. Therefore, there must be two critical Froude numbers Fr_{c1} and Fr_{c2}, and the second vortex linking can only be observed between Fr_{c1} and Fr_{c2}. In this subsection we try to find these two critical Froude numbers.

Figure 22 shows the contours of $\bar{\epsilon}'$ for Fr0.6E0.01ReL, Fr0.7E0.01ReL, Fr0.8E0.01ReL and Fr0.9E0.01ReL. Figure 23 shows the Q isosurfaces for Fr0.6E0.01ReL, Fr0.7E0.01ReL, Fr0.8E0.01ReL at the time we expect to see the vortex linkings. Long-wave instability leads to the first vortex linking in all cases, but the second vortex linking is found in Fr0.8E0.01ReL and Fr0.9E0.01ReL only. Hence, Fr_{c1} is between 0.7 and 0.8. Figure 24 shows the contours of $\bar{\epsilon}'$ for Fr4.0E0.01ReL, Fr6.0E0.01ReL and Fr8.0E0.01ReL. We see the second vortex linking in Fr4.0E0.01ReL and Fr6.0E0.01ReL but not in Fr8.0E0.01ReL ($\bar{\epsilon}'$ does not intensify as in the other two cases). Hence, Fr_{c2} is between 6.0 and 8.0. Further pinpointing of the two critical Froude numbers (to two significant digits) is left for future investigation.

Next, we discuss how the Reynolds number may affect the values of the two critical Froude numbers. Comparing Fr2.0E0.01ReL and Fr2.0E0.01ReM, we notice that the second vortex linking leads to vortex bursts. Since the violent bursts become more violent as the Reynolds number increases, suggesting that it is more likely to observe the second vortex linking at high Reynolds numbers. Hence, Fr_{c1} and Fr_{c2} should decrease and increase slightly as the Reynolds number increases – until the Reynolds number is sufficiently high and these events no longer depend on the Reynolds number.

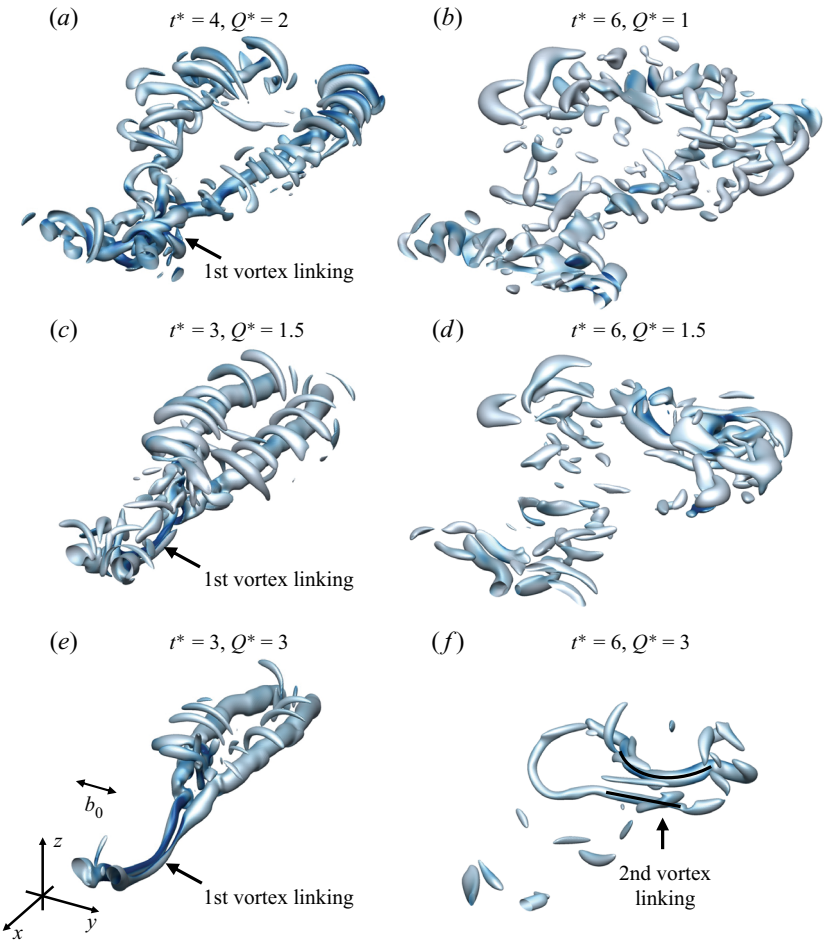

Figure 23. Isosurface of Q^* for case (*a*,*b*) Fr0.6E0.01ReL, (*c*,*d*) Fr0.7E0.01ReL, (*e*,*f*) Fr0.8E0.01ReL. The Q^* isosurfaces at the time of (*a*,*c*,*e*) the first vortex linking, (*b*,*d*) turbulence bursting and (*f*) the second vortex linking.

Likewise, comparing Fr2.0E0.01ReL and Fr2.0E0.10ReL, we note that strong background turbulence distorts the vortices and makes vortex linking (first and second) more difficult. Hence, Fr_{c1} and Fr_{c2} should increase and decrease slightly as the background turbulence increases – until background turbulence completely prevents vortex linking.

4. Conclusions

We conduct DNS to study the evolution of a vortex pair in a stratified and turbulent environment. Direct numerical simulations continue after the long-wave instability completes, and we study the decay of the residual vortices.

In addition to conventional tools like the time histories of the volume integrated dissipation rate and kinetic energy, which contain only temporal information but no spatial information, and Q isosurfaces, which contain only spatial information but no temporal information, the transverse averaged dissipation rate is employed. The transverse averaged

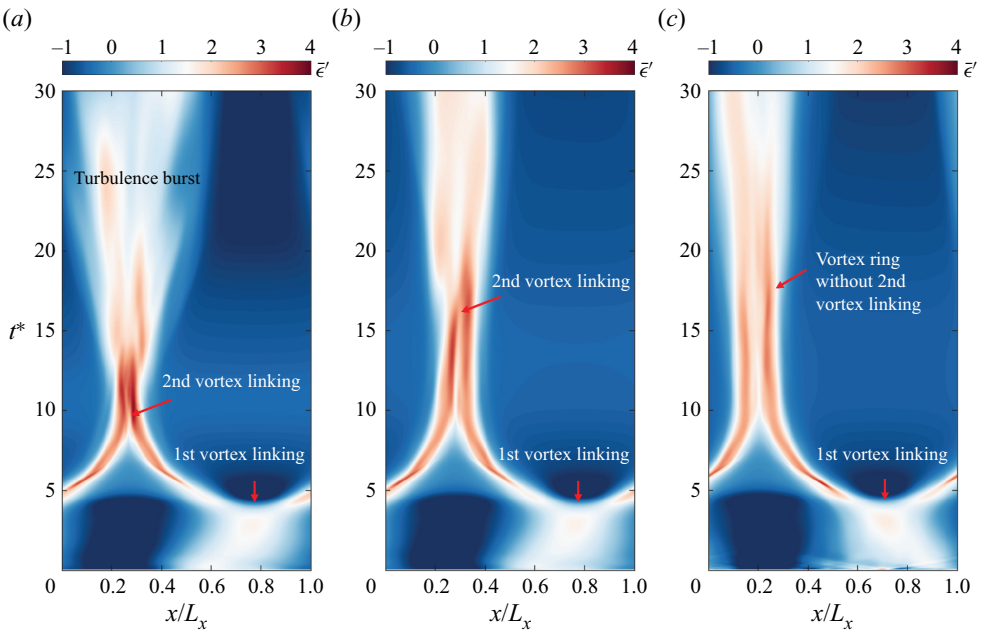

Figure 24. Same as figure 22, but for case (*a*) Fr4.0E0.01ReL, (*b*) Fr6.0E0.01ReL, (*c*) Fr8.0E0.01ReL. Here $\bar{\epsilon}'$ intensifies when the second vortex linking occurs, which happens in (*a*,*b*) but not in (*c*).

dissipation rate contains both temporal and spatial information, and one can easily identify dynamically important events from the plot.

The main finding of the paper is the second vortex linking, which has not been reported before. It occurs after the first vortex linking, i.e. after the Crow instability completes, in a weakly stratified environment when the background turbulence is not very strong. The second vortex linking is followed by turbulence bursts and the rapid decay of residual vortices, the latter of which is responsible for the short life span of the vortex pair. The finding challenges the conventional view that the residual vortices have a long life span, which is only true if the environment is not stratified.

The decay of the residual vortices after the first vortex linking is, in general, poorly understood. In addition to the second vortex linking, our findings include the following. The vortex ring persists for a long time in an unstratified environment in the absence of background turbulence. In a strongly stratified environment, vortex linking is completely prevented, and the vortex pair loses energy to gravitational waves. Background turbulence distorts the vortex ring and helps to dissipate the large eddies in the flow. When the background turbulence is strong, no vortex linking can be observed, and the vortex pair is rapidly torn apart by the background turbulence. Finally, there is no apparent nonlinear interplay between thermal stratification and background turbulence when both are present.

Figure 25 summarizes our data in the Fr–ϵ^* phase space: there exists a regime with no vortex linking (region 1), a regime with the first but not the second vortex linking (region 2) and a regime with both vortex linking events (region 3). More DNS are certainly needed to accurately determine the boundary of these regimes, which is left for future investigation.

We end the paper with a discussion on the practical relevance of this study. The Froude number range investigated in this paper covers the typical flight conditions (Lewellen & Lewellen 1996). The DNS Reynolds number, however, is much lower than the flight Reynolds number, which is $O(10^7)$ per our definition. Direct numerical simulation at

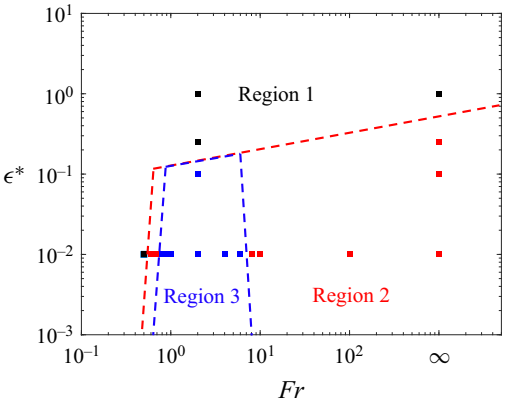

Figure 25. Parameter space. Three regimes can be identified: a regime with no vortex linking (region 1), a regime with the first but not the second vortex linking (region 2), and a regime with both vortex linking events (region 3). The case with no vortex linking is coloured black; the case with the first but not the second vortex linking is coloured red; and the case with both vortex linking events is coloured blue.

that Reynolds number is prohibitively costly and will not be possible in the foreseeable future. The hope is that the basic flow phenomena become Reynolds number independent for Reynolds numbers above a critical value. In this study we compared Fr2.0E0.01ReL and Fr2.0E0.01ReM. The results suggest that the second vortex linking does not depend on the Reynolds number for $Re \gtrsim 10^3$. Hence, the second vortex linking should still be relevant to real-world high-Reynolds-number applications. The Prandtl number effect is not considered in the present study, and we use $Pr = 1$ for all cases. This value is realistic for the atmosphere but unrealistic for the ocean. In oceans Pr maybe 7 for thermal stratification and 700 for salt stratification, the effects of which are left for future investigation.

Acknowledgements. Bin thanks X.L.D. Huang, J.J.L. Li, J. Li and Y. Du for useful inputs.

Funding. X.I.A.Y. acknowledges the support of the Office of Naval Research, contract N000142012315. R.N. acknowledges the support of the Office of Naval Research, contract N000142112123. Y.S. thanks the supported by the National Natural Science Foundation of China, grant number 91752202. Y.Y. acknowledges the partial support from the Marine S&T Fund of Shandong Province for Pilot National Laboratory for Marine Science and Technology (Qingdao) (No.2022QNLM010201).

Declaration of interests. The authors report no conflict of interest.

Author ORCIDs.
Yuanwei Bin https://orcid.org/0000-0001-7722-7885;
Xiang I.A. Yang https://orcid.org/0000-0003-4940-5976;
Yantao Yang https://orcid.org/0000-0001-5065-2769;
Rui Ni https://orcid.org/0000-0002-7178-1479;
Yipeng Shi https://orcid.org/0000-0002-1688-1848.

Appendix A. A validation

We present a validation study and compare our DNS to that in Garten *et al.* (2001) at $Fr = \infty$, i.e. unstratified, and $Re = 942$. At this condition, the two vortices deform as a result of the Crow instability (Crow 1970). Figure 26 is a sketch of one vortex before they link. The other vortex is to the left of the centre plane at $y = 0$ and is not plotted in figure 26

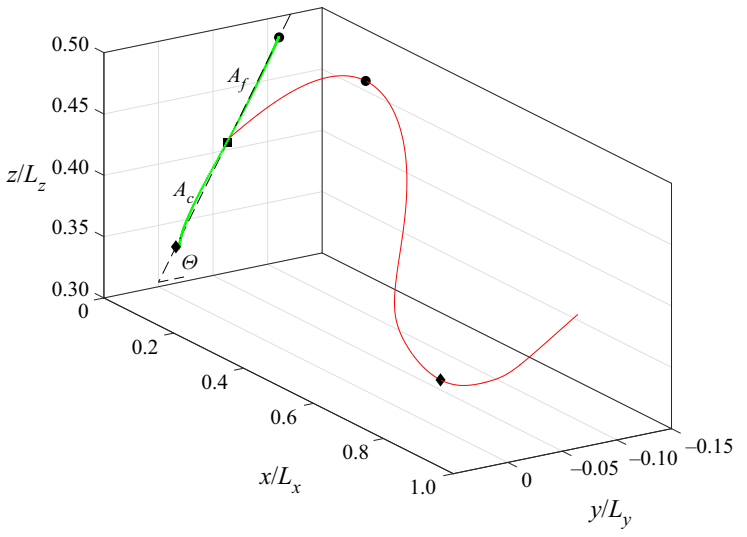

Figure 26. A sketch of one of the two vortices (red line) before reconnection. The green line is the projection of the vortex on the y–z plane. The circle, triangle and square mark the two ends and the mid-point of the line. Here $L = 8.6b$ and Θ is the angle between the projection and the y axis.

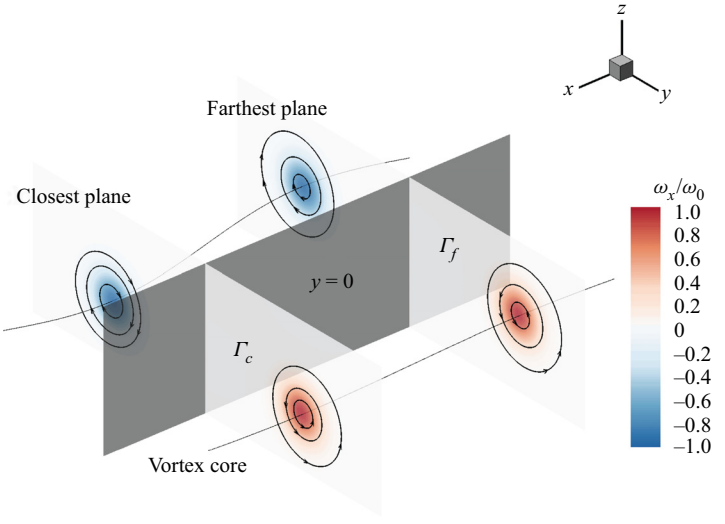

Figure 27. A sketch of the flow fields across the two hollow symbols.

for visualization purposes. The projection of the vortex on the y–z plane is approximately a straight line. Its centre is indicated with a filled square symbol in figure 26, and the two ends are indicated with a filled triangle and a filled circle. The triangle symbol marks the location where the distance between the two vortices is the closest, and the circle symbol marks the point where the two vortices are the farthest. We use A_c to denote the distance between the triangle and the square and A_f to denote the distance between the circle and the square. Besides A_c and A_f, Θ denotes the angle between the projection of the vortex and the y axis. Figure 27 is a sketch of the flow fields across the circle and the triangle symbols. We can compute the circulation by integrating the velocity along the y–z plane

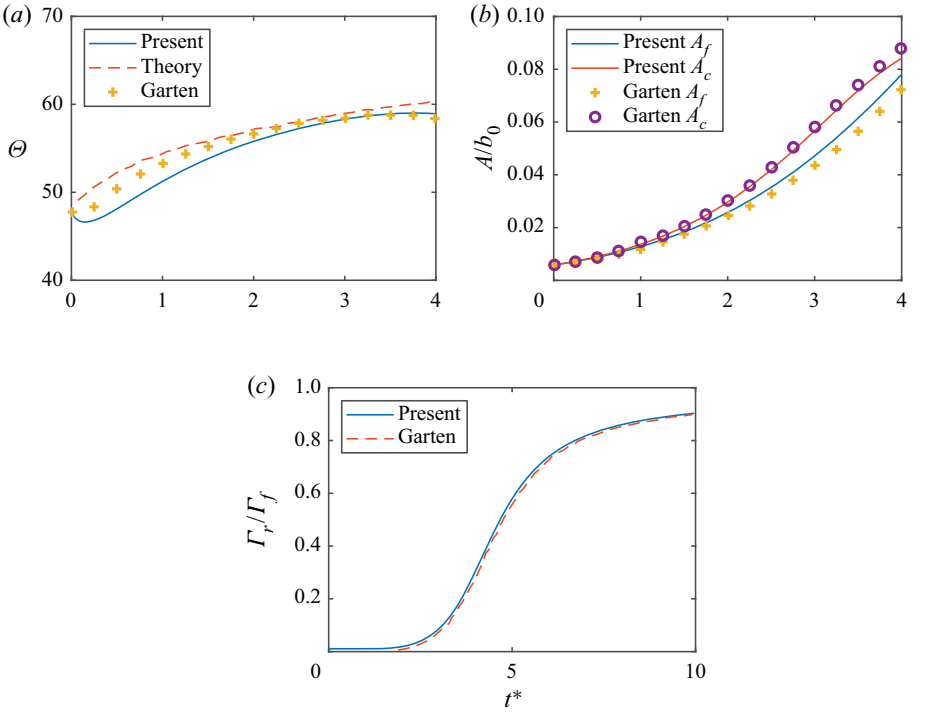

Figure 28. Evolution of (*a*) Θ, (*b*) A_c, A_f and (*c*) Γ_r/Γ_f as a function of time.

where x equals a constant and $y > 0$, i.e.

$$\Gamma(x) = \int_0^{L_y/2} \int_0^{L_z} \omega_x(x, y, z)\, \mathrm{d}y\, \mathrm{d}z. \tag{A1}$$

The Crow instability leads to relatively weak circulation in the closest plane and relatively strong circulation in the farthest plane, where two planes are shown in figure 27. We denote the circulations on these two planes as Γ_f and Γ_c and define $\Gamma_r = \Gamma_f - \Gamma_c$.

Figure 28(*a–c*) compares the evolution of Θ, A_f, A_c and Γ_r/Γ_f in our DNS and Garten *et al.* (2001)'s DNS. The theoretical predictions by Crow (1970) are plotted in figure 28(*a*) as references. We see that both DNS follow the theoretical predictions quite closely. A detailed discussion of these flow quantities and their behaviours is not the purpose of this validation study, and it is not pursued here.

References

Agrawal, R. & Chandy, A.J. 2021 Large eddy simulations of forced and stably stratified turbulence: evolution, spectra, scaling, structures and shear. *Intl J. Heat Fluid Flow* **89**, 108778.

Billant, P. 2010 Zigzag instability of vortex pairs in stratified and rotating fluids. Part 1. General stability equations. *J. Fluid Mech.* **660**, 354–395.

Billant, P., Deloncle, A., Chomaz, J.-M. & Otheguy, P. 2010 Zigzag instability of vortex pairs in stratified and rotating fluids. Part 2. Analytical and numerical analyses. *J. Fluid Mech.* **660**, 396–429.

Chung, D. & Matheou, G. 2012 Direct numerical simulation of stationary homogeneous stratified sheared turbulence. *J. Fluid Mech.* **696**, 434–467.

Crouch, J.D. 1997 Instability and transient growth for two trailing-vortex pairs. *J. Fluid Mech.* **350**, 311–330.

Crow, S.C. 1974 Motion of a vortex pair in a stably stratified fluid. *Poseidon Res. Rep.* **1**.

Crow, S.C. 1970 Stability theory for a pair of trailing vortices. *AIAA J.* **8** (12), 2172–2179.

CROW, S.C. & BATE, E.R. 1976 Lifespan of trailing vortices in a turbulent atmosphere. *J. Aircraft* **13** (7), 476–482.

DE VISSCHER, I., BRICTEUX, L. & WINCKELMANS, G. 2013 Aircraft vortices in stably stratified and weakly turbulent atmospheres: simulation and modeling. *AIAA J.* **51** (3), 551–566.

DU, Y., ZHANG, M. & YANG, Y. 2021 Two-component convection flow driven by a heat-releasing concentration field. *J. Fluid Mech.* **929**, A35.

GARTEN, J.F., ARENDT, S., FRITTS, D.C. & WERNE, J. 1998 Dynamics of counter-rotating vortex pairs in stratified and sheared environments. *J. Fluid Mech.* **361**, 189–236.

GARTEN, J.F., WERNE, J., FRITTS, D.C. & ARENDT, S. 2001 Direct numerical simulations of the crow instability and subsequent vortex reconnection in a stratified fluid. *J. Fluid Mech.* **426**, 1–45.

GERZ, T., HOLZÄPFEL, F. & DARRACQ, D. 2002 Commercial aircraft wake vortices. *Prog. Aerosp. Sci.* **38** (3), 181–208.

GREENE, G.C. 1986 An approximate model of vortex decay in the atmosphere. *J. Aircraft* **23** (7), 566–573.

HAN, J., LIN, Y.-L., SCHOWALTER, D.G., ARYA, S.P. & PROCTOR, F.H. 2000*a* Large eddy simulation of aircraft wake vortices within homogeneous turbulence: Crow instability. *AIAA J.* **38** (2), 292–300.

HAN, J., LIN, Y.-L., SCHOWALTER, D.G., ARYA, S.P. & PROCTOR, F.H. 2000*b* Within homogeneous turbulence: crow instability large eddy simulation of aircraft wake vortices. *AIAA J.* **38** (2), 292–300.

HECHT, A.M., BILANIN, A.J. & HIRSH, J.E. 1981 Turbulent trailing vortices in stratified fluids. *AIAA J.* **19** (6), 691–698.

HILL, F.M. 1975 A numerical study of the descent of a vortex pair in a stably stratified atmosphere. *J. Fluid Mech.* **71** (1), 1–13.

HOLZÄPFEL, F. & GERZ, T. 1999 Two-dimensional wake vortex physics in the stably stratified atmosphere. *Aerosp. Sci. Technol.* **3** (5), 261–270.

HOLZÄPFEL, F., HOFBAUER, T., DARRACQ, D., MOET, H., GARNIER, F. & GAGO, C.F. 2003 Analysis of wake vortex decay mechanisms in the atmosphere. *Aerosp. Sci. Technol.* **7** (4), 263–275.

HOLZÄPFEL, F., GERZ, T. & BAUMANN, R. 2001 The turbulent decay of trailing vortex pairs in stably stratified environments. *Aerosp. Sci. Technol.* **5** (2), 95–108.

HUSSAIN, F. & DURAISAMY, K. 2011 Mechanics of viscous vortex reconnection. *Phys. Fluids* **23** (2), 021701.

VAN JAARSVELD, J.P.J., HOLTEN, A.P.C., ELSENAAR, A., TRIELING, R.R. & VAN HEIJST, G.J.F. 2011 An experimental study of the effect of external turbulence on the decay of a single vortex and a vortex pair. *J. Fluid Mech.* **670**, 214–239.

JI, L. & VAN REES, W.M. 2022 Bursting on a vortex tube with initial axial core-size perturbations. *Phys. Rev. Fluids* **7** (4), 044704.

KERR, R.M. & HUSSAIN, F. 1989 Simulation of vortex reconnection. *Physica* D **37** (1–3), 474–484.

KIM, J. & MOIN, P. 1985 Application of a fractional-step method to incompressible Navier–Stokes equations. *J. Comput. Phys.* **59** (2), 308–323.

KLEIN, R., MAJDA, A.J. & DAMODARAN, K. 1995 Simplified equations for the interaction of nearly parallel vortex filaments. *J. Fluid Mech.* **288**, 201–248.

LAPORTE, F. & CORJON, A. 2000 Direct numerical simulations of the elliptic instability of a vortex pair. *Phys. Fluids* **12** (5), 1016–1031.

LEWEKE, T., LE DIZÈS, S. & WILLIAMSON, C.H.K. 2016 Dynamics and instabilities of vortex pairs. *Annu. Rev. Fluid Mech.* **48** (1), 507–541.

LEWEKE, T. & WILLIAMSON, C.H.K. 1998 Cooperative elliptic instability of a vortex pair. *J. Fluid Mech.* **360**, 85–119.

LEWEKE, T. & WILLIAMSON, C.H.K. 2011 Experiments on long-wavelength instability and reconnection of a vortex pair. *Phys. Fluids* **23** (2), 024101.

LEWELLEN, D.C. & LEWELLEN, W.S. 1996 Large-eddy simulations of the vortex-pair breakup in aircraft wakes. *AIAA J.* **34** (11), 2337–2345.

LEWELLEN, D.C., LEWELLEN, W.S., POOLE, L.R., DECOURSEY, R.J., HANSEN, G.M., HOSTETLER, C.A. & KENT, G.S. 1998 Large-eddy simulations and lidar measurements of vortex-pair breakup in aircraft wakes. *AIAA J.* **36** (8), 1439–1445.

LI, J. & YANG, Y. 2021 Thermohaline interleaving induced by horizontal temperature and salinity gradients from above. *J. Fluid Mech.* **927**, A12.

MCGOWAN, W.A. 1968 Trailing vortex hazard. *SAE Trans.* **77**, 740–753.

MCKEOWN, R., OSTILLA-MÓNICO, R., PUMIR, A., BRENNER, M.P. & RUBINSTEIN, S.M. 2020 Turbulence generation through an iterative cascade of the elliptical instability. *Sci. Adv.* **6** (9), eaaz2717.

MELANDER, M.V. & HUSSAIN, F. 1989 Cross-linking of two antiparallel vortex tubes. *Phys. Fluids* A **1** (4), 633–636.

MELANDER, M.V. & HUSSAIN, F. 1988 Cut-and-connect of two antiparallel vortex tubes. In *Stanford Univ., Studying Turbulence Using Numerical Simulation Databases, 2. Proceedings of the 1988 Summer Program*.

MISAKA, T., HOLZÄPFEL, F., HENNEMANN, I., GERZ, T., MANHART, M. & SCHWERTFIRM, F. 2012 Vortex bursting and tracer transport of a counter-rotating vortex pair. *Phys. Fluids* **24** (2), 025104.

MISHRA, A., PUMIR, A. & OSTILLA-MÓNICO, R. 2021 Instability and disintegration of vortex rings during head-on collisions and wall interactions. *Phys. Rev. Fluids* **6** (10), 104702.

MOET, H., DARRACQ, D., LAPORTE, F. & CORJON, A. 2000 Investigation of ambient turbulence effects on vortex evolution using LES. In *38th Aerospace Sciences Meeting and Exhibit, AIAA Paper* 2012-0756.

MOORE, D.W. & SAFFMAN, P.G. 1975 The instability of a straight vortex filament in a strain field. *Proc. R. Soc. Lond.* A **346** (1646), 413–425.

NELSON, R. 2004 The trailing vortex wake hazard: beyond the takeoff and landing corridors. In *AIAA Atmospheric Flight Mechanics Conference and Exhibit, AIAA Paper* 2004-5171.

NOMURA, K.K., TSUTSUI, H., MAHONEY, D. & ROTTMAN, J.W. 2006 Short-wavelength instability and decay of a vortex pair in a stratified fluid. *J. Fluid Mech.* **553**, 283–322.

ORTIZ, S., DONNADIEU, C. & CHOMAZ, J.-M. 2015 Three-dimensional instabilities and optimal perturbations of a counter-rotating vortex pair in stratified flows. *Phys. Fluids* **27** (10), 106603.

OSTILLA-MÓNICO, R., MCKEOWN, R., BRENNER, M.P., RUBINSTEIN, S.M. & PUMIR, A. 2021 Cascades and reconnection in interacting vortex filaments. *Phys. Rev. Fluids* **6** (7), 074701.

OSTILLA-MONICO, R., YANG, Y., VAN DER POEL, E.P., LOHSE, D. & VERZICCO, R. 2015 A multiple-resolution strategy for direct numerical simulation of scalar turbulence. *J. Comput. Phys.* **301**, 308–321.

VAN DER POEL, E.P., OSTILLA-MÓNICO, R., DONNERS, J. & VERZICCO, R. 2015 A pencil distributed finite difference code for strongly turbulent wall-bounded flows. *Comput. Fluids* **116**, 10–16.

PUMIR, A. & KERR, R.M. 1987 Numerical simulation of interacting vortex tubes. *Phys. Rev. Lett.* **58** (16), 1636.

PUMIR, A. & SIGGIA, E. 1990 Collapsing solutions to the 3-D Euler equations. *Phys. Fluids* A **2** (2), 220–241.

VAN REES, W.M., HUSSAIN, F. & KOUMOUTSAKOS, P. 2012 Vortex tube reconnection at $Re = 10^4$. *Phys. Fluids* **24** (7), 075105.

ROBINS, R.E. & DELISI, D.P. 1998 Numerical simulation of three-dimensional trailing vortex evolution in stratified fluid. *AIAA J.* **36** (6), 981–985.

SAFFMAN, P.G. 1972 The motion of a vortex pair in a stratified atmosphere. *Stud. Appl. Maths* **51** (2), 107–119.

SAFFMAN, P.G. 1990 A model of vortex reconnection. *J. Fluid Mech.* **212**, 395–402.

SARPKAYA, T. 1983 Trailing vortices in homogeneous and density-stratified media. *J. Fluid Mech.* **136**, 85–109.

SHELLEY, M.J., MEIRON, D.I. & ORSZAG, S.A. 1993 Dynamical aspects of vortex reconnection of perturbed anti-parallel vortex tubes. *J. Fluid Mech.* **246**, 613–652.

SPALART, P.R. 1996 On the motion of laminar wing wakes in a stratified fluid. *J. Fluid Mech.* **327**, 139–160.

SPALART, P.R. 1998 Airplane trailing vortices. *Annu. Rev. Fluid Mech.* **30** (1), 107–138.

SWITZER, G. & PROCTOR, F. 2002 Wake vortex prediction models for decay and transport within stratified environments. In *40th AIAA Aerospace Sciences Meeting & Exhibit, AIAA Paper* 2002-945.

TSAI, C.-Y. & WIDNALL, S.E. 1976 The stability of short waves on a straight vortex filament in a weak externally imposed strain field. *J. Fluid Mech.* **73** (4), 721–733.

WIDNALL, S.E. 1975 The structure and dynamics of vortex filaments. *Annu. Rev. Fluid Mech.* **7** (1), 141–165.

YANG, Y., CHEN, W., VERZICCO, R. & LOHSE, D. 2020 Multiple states and transport properties of double-diffusive convection turbulence. *Proc. Natl Acad. Sci. USA* **117** (26), 14676–14681.

YANG, Y., VAN DER POEL, E.P., OSTILLA-MÓNICO, R., SUN, C., VERZICCO, R., GROSSMANN, S. & LOHSE, D. 2015 Salinity transfer in bounded double diffusive convection. *J. Fluid Mech.* **768**, 476–491.

YAO, J. & HUSSAIN, F. 2020 A physical model of turbulence cascade via vortex reconnection sequence and avalanche. *J. Fluid Mech.* **883**, A51.

YAO, J. & HUSSAIN, F. 2022 Vortex reconnection and turbulence cascade. *Annu. Rev. Fluid Mech.* **54**, 317–347.